

Semi-Annual Report Submitted to the
National Aeronautics and Space Administration

For January - June, 1996

1N71R112
1N-43-CR
OC 11
67204

Contract Number: NAS5-31370
Land Surface Temperature Measurements
from EOS MODIS Data

MODIS Team Member
PRINCIPAL INVESTIGATOR

ZHENGMING WAN

P.I.'s Address:

ZHENGMING WAN
Institute for Computational Earth System Science
University of California
Santa Barbara, CA 93106-3060

phone : (805) 893-4541
Fax no: (805) 893-2578
Internet: wan@icess.ucsb.edu

Land Surface Temperature Measurements from EOS MODIS Data

Semi-Annual Report
For January - June, 1996

Zhengming Wan
Contract Number: NAS5-31370

Abstract

A substantive progress has been made in the development of the new MODIS day/night land-surface temperature (LST) algorithm which retrieves surface emissivity and temperature simultaneously for land covers with variable emissivities. The assumptions of surface BRDF and reflectance in the 3-14 μ m range which we made in the LST algorithm have been validated by our spectral BRDF measurements in the thermal infrared. The physical principle of this day/night LST algorithm has been validated by ground-based measurements with the sun/shadow method. Comprehensive sensitivity and error analysis shows that the day/night LST algorithm is not very sensitive to uncertainties in the instrument noise and calibration accuracy and that the standard deviations of errors in retrieved surface daytime and nighttime temperatures are better than 0.8°K, and the standard deviations of errors in retrieved emissivities in MODIS bands 31 and 32 (located at 11 μ m and 12 μ m) are better than 0.01 over wide ranges of atmospheric and surface conditions.

The version 1 of the MODIS LST software is being prepared for its delivery scheduled in the early second half of this year.

1. Recent Progress in TIR Instrumentation

A substantive progress has been made in the development of the new MODIS day/night land-surface temperature (LST) algorithm which retrieves surface emissivity and temperature simultaneously for land covers with variable emissivities. Comprehensive sensitivity and error analysis shows that the day/night LST algorithm is not very sensitive to uncertainties in the instrument noise and calibration accuracy and that the standard deviations of errors in retrieved surface daytime and nighttime temperatures are better than 0.8°K , and the standard deviations of errors in retrieved emissivities in MODIS bands 31 and 32 (located at $11\mu\text{m}$ and $12\mu\text{m}$) are better than 0.01 over wide ranges of atmospheric and surface conditions. A paper on this new LST algorithm has been submitted to the peer review journal IEEE Trans. Geoscience and Remote Sensing, and the manuscript has been revised according to peer reviewer's comments. We included this revised manuscript in Appendix I.

The assumptions of surface BRDF and reflectance in the $3\text{-}14\mu\text{m}$ range which we made in the day/night LST algorithm have been validated by our spectral BRDF measurements in the thermal infrared. A paper on TIR BRDF measurements of sands and soils has been submitted to the peer review journal Remote Sensing of Environment, and the manuscript has been revised and resubmitted to the editor. We include this revised manuscript in Appendix II.

The physical principle of this day/night LST algorithm has been validated by ground-based measurements with the sun/shadow method. A paper on this sun/shadow method has been submitted to the peer review journal IEEE Trans. Geoscience and Remote Sensing in March 1996.

Two field campaigns were conducted in order to validate the LST algorithms. The first field campaign was conducted in a snow cover test site in Mammoth Lake area in April 2, 1996. The second field campaign was conducted jointly with other groups in Railroad Valley, Nevada in June 4, 1996. MODIS Airborne Simulator flights and ground-based TIR spectral measurements were accomplished in these two field campaigns.

2. V1 Delivery of the MODIS LST Code

Two MODIS LST algorithms have been developed. Toolkit software packages of Product Generation System (PGS) and MODIS Application Program Interface (M-API) have been implemented on local SCF (Science Computing Facility) DEC Alpha workstations. The V1 version of the MODIS LST code is being prepared for its delivery scheduled in the early second half of this year.

3. Anticipated Future Actions

The MODIS LST ATBD (Algorithm Theoretical Base Document) will be revised before August 16th. MAS data and field measurement data collected in the last two field campaigns will be used to validate the MODIS LST algorithms. V1 version of the MODIS LST code will be delivered. The work to establish TIR BRDF/emissivity knowledge base and the development of MODIS LST algorithm will be continued.

4. Publications

1. Z. Wan and J. Dozier, "A generalized split-window algorithm for retrieving land-surface temperature from space", IEEE Trans. Geosci. Remote Sens., vol. 34, no. 4, pp. 892-905, 1996.
2. W. Snyder and Z. Wan, "Surface temperature correction for active infrared reflectance measurements of natural materials", Appl. Optics, vol. 35, no. 13, pp. 2216-2220, 1996.
3. Z. Wan, W. Snyder and Y. Zhang, "Validation of land-surface temperature retrieval from space", Proc. IGARSS '96, pp. 2095-2097, 1996.
4. Z. Wan and Z.-L. Li, "A physics-based algorithm for retrieving land-surface emissivity and temperature from EOS/MODIS data", IEEE Trans. Geosci. Remote Sens., revised 1996.
5. W. Snyder, Z. Wan, Y. Zhang and Y.-Z. Feng, "Thermal infrared (3-14 μ m) bidirectional reflectance measurements of sands and soils", Remote Sens. Environ., revised 1996.
6. Z. Wan, W. Snyder, Z.-L. Li, Y. Zhang and Y.-Z. Feng, "A sun-shadow method for in-situ measurements of land-surface temperature and emissivity", IEEE Trans. Geosci. Remote Sens., submitted 1996.

Appendix I

Z. Wan and Z.-L. Li, "A physics-based algorithm for retrieving land-surface emissivity and temperature from EOS/MODIS data", IEEE Trans. Geosci. Remote Sens., revised 1996.

Appendix II

W. Snyder, Z. Wan, Y. Zhang and Y.-Z. Feng, "Thermal infrared (3-14 μm) bidirectional reflectance measurements of sands and soils", Remote Sens. Environ., revised 1996.

A PHYSICS-BASED ALGORITHM FOR RETRIEVING LAND-SURFACE EMISSIONIVITY AND TEMPERATURE FROM EOS/MODIS DATA

Zhengming Wan ¹⁾ and Zhao-Liang Li ²⁾

1) ICES, University of California, Santa Barbara, CA 93106-3060, USA

2) GRTR/LSIT/CNRS (URA 1871), 67400 Illkirch-Graffenstaden, France

Abstract — We have developed a physics-based land-surface temperature (LST) algorithm for simultaneously retrieving surface band-averaged emissivities and temperatures from day/night pairs of MODIS (Moderate Resolution Imaging Spectroradiometer) data in 7 thermal infrared bands. The set of 14 nonlinear equations in the algorithm is solved with the statistical regression method and the least-squares fit method. This new LST algorithm was tested with simulated MODIS data for 80 sets of band-averaged emissivities calculated from published spectral data of terrestrial materials in wide ranges of atmospheric and surface temperature conditions. Comprehensive sensitivity and error analysis has been made to evaluate the performance of the new LST algorithm and its dependence on variations in surface emissivity and temperature, on atmospheric conditions, and on the noise-equivalent temperature difference (NE Δ T) and calibration accuracy specifications of the MODIS instrument. In cases with a systematic calibration error of 0.5%, the standard deviations of errors in retrieved surface daytime and nighttime temperatures fall between 0.4-0.5°K over a wide range of surface temperatures for mid-latitude summer conditions. The standard deviations of errors in retrieved emissivities in bands 31 and 32 are 0.009, and the maximum error in retrieved LST values falls between 2-3°K.

1. INTRODUCTION

Land-surface temperature (LST) is one of the key parameters in the physics of land-surface processes on regional and global scales, combining the results of all surface-atmosphere interactions and energy fluxes between the atmosphere and the ground [1, 2]. Therefore it is required for a wide variety of climatic, hydrological, ecological and biogeochemical studies [3, 4]. In order to understand

the entire Earth system better on the global scale, the Earth Observing System (EOS) will provide surface kinetic temperatures at specified accuracies of 0.3°K for oceans and 1°K over land. The international Tropical Ocean Global Atmosphere (TOGA) program has specified that sea surface temperature (SST) should be accurate to 0.3°K for global numerical models of climate.

During the past decade, significant progress has been made in estimation of land-surface emissivity and temperature from airborne thermal infrared data. Kahle et al. [5] developed a technique to estimate the surface temperature based on an assumed constant emissivity in one channel and previously determined atmospheric parameters; this temperature was then used to estimate the emissivity in other channels [6]. Other techniques, such as thermal log residuals and alpha residuals, have been recently developed to extract emissivity information from multispectral thermal infrared data [7].

A variety of split-window methods have been developed to retrieve sea-surface temperature and land-surface temperature from NOAA AVHRR data. The split-window LST method corrects the atmospheric effects based on the differential absorption in adjacent infrared bands [8, 9, 10, 11, 12, 13, 14, 15, 16, 17]. A major problem in using split-window LST methods is that we need to know the surface emissivities in the bands to better than 0.01. It seems possible to have such knowledge of the emissivities for certain types of land covers, such as lake surfaces, snow/ice covers, dense evergreen canopies, and some soils. For land covers with variable emissivities, especially in semi arid and arid areas, it is almost impossible to estimate two band-averaged emissivities to such accuracy, so it is necessary to develop new algorithms to retrieve LST without prior knowledge of surface emissivities. In addition, surface emissivity is also needed to calculate up-welling thermal infrared radiation, and for environmental monitoring and geological mapping [5].

Li and Becker [18] proposed a method to estimate both land-surface emissivity and LST using pairs of day/night co-registered AVHRR images. They used a temperature-independent spectral index (TISI) in thermal infrared bands and assumed knowledge of surface TIR BRDF (thermal infrared Bidirectional Reflectance Distribution Function) and atmospheric profiles. Such combined a priori knowledge and information are not readily available in most situations.

MODIS is an EOS instrument that will serve as the keystone [19] for global studies of atmosphere [20], land [4], and ocean processes. It scans $\pm 55^\circ$ from nadir in 36 bands, with bands 1-19 and band 26 in the visible and near infrared range, and the remaining bands in the thermal infrared from 3 to $15\ \mu\text{m}$. The specifications of MODIS bands are shown in Table I. We used the updated atmospheric radiative transfer model, MODTRAN3 code [21], to calculate spectral atmospheric transmission in a typical mid-latitude summer clear-sky condition, where column water vapor is 2.9cm and visibility at surface is 23km. Viewing angle is selected at 45° . Figure 1 shows the total transmission and transmission functions corresponding to water vapor (H_2O) band absorption and continuum absorption, uniformly mixed gases (CO_2 +) and ozone absorptions. The transmission functions corresponding to molecular scattering, aerosol scattering and absorption are also shown in this figure. By checking the atmospheric transmission functions, we can have some general ideas for applications of the MODIS bands. Those bands in transparent atmospheric windows are designed for remote sensing of surface properties. Other bands are mainly for atmospheric studies. The exact location and bandwidth of MODIS bands are selected to meet the requirements from atmospheric, ocean and land sciences. MODIS will provide images of daylight reflection and day/night emission of the Earth every 1-2 days. It uses 12 bits for quantization in all bands. The thermal infrared bands have an IFOV (instantaneous field-of-view) of about 1 km at nadir. MODIS will view cold space and a full-aperture blackbody before and after viewing the Earth scene in order to achieve calibration accuracy of better than 1% absolute for thermal infrared bands. MODIS is particularly useful because of its global coverage, radiometric resolution and dynamic ranges, and accurate calibration in multiple thermal infrared bands designed for retrievals of SST, LST and atmospheric properties. Specifically, bands 3-7, 13, and 16-19 will be used to classify land-cover to infer emissivities, band 26 will detect cirrus clouds, and thermal infrared bands 20, 22, 23, 29, 31-33 will correct for atmospheric effects and retrieve surface emissivity and temperature. The atmospheric sounding channels of MODIS will be used to retrieve atmospheric temperature and water vapor profiles [22]. Multiple bands in the mid-infrared range will provide, for the first time, corrections for solar radiation in daytime LST estimations using mid-infrared data. Because of its multiple bands in the mid-infrared range and in the $8\text{-}14\ \mu\text{m}$ window, MODIS provides an unprecedented opportunity to develop a physics-based algorithm to simultaneously retrieve surface emissivity and temperature. In Section II, we present the theoretical basis of the new LST algorithm. Section III describes numerical

methods used in the algorithm. Section IV gives simulation results of the new LST algorithm and results from sensitivity and error analysis. Finally, conclusions are given in Section V.

II. THEORETICAL-BASIS OF THE NEW LST ALGORITHM

For land covers with variable and unknown emissivities, obviously there is insufficient information (mathematically under-determined) to retrieve surface temperature and band-averaged emissivities from a one-time measurement of N thermal infrared channels even when atmospheric temperature and humidity profiles are known exactly (we know that it is impossible), because there are $N + 1$ unknowns (N band emissivities plus surface temperature). Therefore, we will consider using multi-temporal and multi-channel data.

A. A Physics-Based Day/Night LST Model

In clear-sky conditions, the spectral infrared radiance $L(\lambda, \mu)$ at the top of the atmosphere is composed of surface thermal emittance, thermal path radiance $L_a(\lambda, \mu)$, path radiance resulting from scattering of solar radiation $L_s(\lambda, \mu, \mu_0, \phi_0)$, solar beam and downward solar diffuse radiation and atmospheric thermal radiation reflected by the surface,

$$L(\lambda, \mu) = t_1(\lambda, \mu) \varepsilon(\lambda, \mu) B(\lambda, T_s) + L_a(\lambda, \mu) + L_s(\lambda, \mu, \mu_0, \phi_0) + t_2(\lambda, \mu, \mu_0) \mu_0 E_0(\lambda) f_r(\mu; \mu_0, \phi_0) + \int_0^{2\pi} \int_0^1 \mu' f_r(\mu; \mu', \phi') [t_3(\lambda, \mu) L_d(\lambda, -\mu', \phi') + t_4(\lambda, \mu) L_t(\lambda, -\mu', \phi')] d\mu' d\phi', \quad (1)$$

where μ is cosine of the viewing zenith angle, $\varepsilon(\lambda, \mu)$ is the surface spectral emissivity, $B(\lambda, T_s)$ is the radiance emitted by a blackbody at surface temperature T_s , $E_0(\lambda)$ is the spectral solar irradiance incident on the top of the atmosphere (normal to the beam), μ_0 is cosine of the solar zenith angle, ϕ_0 is the relative azimuth between the viewing direction and the solar beam direction, $f_r(\mu; \mu', \phi')$ is the BRDF function, $L_d(\lambda, -\mu', \phi')$ is the downward solar diffuse radiance, $L_t(\lambda, -\mu', \phi')$ is the atmospheric downward thermal radiance, their incident direction is represented by $-\mu'$ and ϕ' , and $t_i()$, $i = 1, \dots, 4$ are transmission functions for the corresponding terms.

The wavelength, λ , in (1) is the wavelength center of a narrow wavelength interval because there is no way to measure the exact monochromatic signal as a continuous function of wavelength by satellite sensors. Equation (1) is the generalized form used in the thermal infrared range 8-14 μm [23] into a wider wavelength range of 3-14 μm . It requires complete calculations of the atmospheric radiative transfer to determine the values of all terms on the right-hand side. After the zenith and azimuth dependent radiance at any levels from the Earth's surface to the top of the atmosphere (TOA) is provided by accurate atmospheric radiative transfer simulations, the TOA radiance can be represented by its components in form (1). Its special form has been used for a long time in many atmospheric radiation models including LOWTRAN [24], MODTRAN [25], and MOSART models [26]. In the special form, $t_3(\lambda, \mu) = t_1(\lambda, \mu)$ and $t_4(\lambda, \mu) = t_1(\lambda, \mu)$ are assumed.

In order to retrieve surface emissivity and temperature from (1), we need to use suitable TIR bands. According to the MODIS band specifications in Table I and the atmospheric transmission in Figure 1, bands 20, 22, and 23 are in the transparent atmospheric window in the medium wavelength range 3.5-4.2 μm , bands 29-32 are in the atmospheric window range 8-13 μm , while band 33 is just on the edge of this atmospheric window. Band 30 is strongly affected by ozone absorption, so using this band does not help to retrieve surface temperature. As shown in Figure 1, major absorbers in bands 20, 22, and 23 are CO_2 , N_2 , and water vapor. Major absorbers in bands 29, and 31-33 are water vapor and CO_2 . The transmission corresponding to aerosol scattering and absorption in these bands is about 0.95-0.98. So using average aerosol distribution in atmospheric radiative transfer is usually good enough unless volcano eruptions strongly change the aerosol distribution. Since CO_2 and O_2 mixing ratios are almost constant, their densities are determined by atmospheric pressure and temperature. Water vapor is the most variable absorber in the Earth's atmosphere. Therefore, if we know atmospheric water vapor and temperature profiles, we can calculate all atmospheric terms in the above equation to a quite high accuracy, which is limited mainly by the accuracy of the coefficients of the water vapor continuum and band absorptions. The MODIS sounding channels can be used to retrieve atmospheric temperature and water vapor profiles [22, 27]. But retrieving atmospheric profiles needs the knowledge of surface emissivity in order to separate the surface contribution from the sounding data. Therefore, the quality of retrieved profiles might not be very good in areas where surface emissivities are highly variable such

as in semi-arid and arid areas. Although the absolute values of the retrieved profiles are not accurate, the shapes of the atmospheric temperature and water vapor profiles may be reasonably well obtained. Radiative transfer simulations show that the radiance at the top of the atmosphere, in MODIS TIR bands 20, 22, 23, 29, 31-33, is almost not affected by changing atmospheric temperature and water vapor profiles at levels above elevation 9km. If the shapes of temperature and water vapor profiles in the lower troposphere can be well retrieved from the MODIS sounding data, we can use two variables to describe the atmospheric variations. One is the amount of shift in the temperature profile up to elevation 9km. Another is the scale factor for the water vapor profile so that we can determine the column water vapor with the shape and the scale factor. Then we use the atmospheric temperature at the surface level, T_a , as the representative variable of the tropospheric temperature profile. Similarly, we can use the column water vapor (cwv) as the representative for the water vapor profile. Alternatively, we can consider it as the first order of approximation to describe the atmospheric condition by using these two variables.

In order to make practical use of multi-temporal and multi-channel data, we need to simplify (1) by using some realistic assumptions about the surface optical properties. We assume: 1) The surface emissivity changes with vegetation coverage and surface moisture content, but it does not significantly change in several days unless rain and/or snow occurs during the short period of time particularly for bare soils in arid and semi-arid environments, for which the surface of the ground is dry most of time [14]. 2) There are quite strong spectral variations in surface reflectance for most terrestrial materials in the medium wavelength range 3.5-4.2 μm [28] but their BRDF anisotropic factor in this wavelength range has very small variations in the order of 2% [29, 30]. So it seems appropriate to assume that a single BRDF anisotropic factor can be used for the surface-reflected solar beam in MODIS bands 20, 22 and 23 located in this wavelength range. This anisotropic factor is defined by the ratio of the surface-reflected solar beam at the view direction of the MODIS sensor to the radiance that would have resulted if the surface reflected isotropically (such a surface is called Lambertian surface),

$$\alpha = \frac{\pi f_r(\mu; \mu_0, \phi_0)}{r}, \quad (2)$$

where r is reflectance of the assumed Lambertian surface. 3) Atmospheric radiative transfer

simulations show that in clear-sky conditions the surface-reflected diffuse solar irradiance term is much smaller than the surface-reflected solar beam term in the thermal infrared range, and the surface-reflected atmospheric downward thermal irradiance term is smaller than surface thermal emission. So the Lambertian approximation of the surface reflection does not introduce a significant error in thermal infrared region 3-14 μm . Then we can replace the BRDF function $f_r(\mu, \mu', \phi')$ in (1) with r/π and link it to the surface emissivity ϵ by $r = 1 - \epsilon$ according to the Kirchhoff's law.

It is important to point out that in (1) we separate the surface-reflected solar beam term from its irradiance term (the integral of the downward solar diffuse radiance) because changing solar zenith angle has different effects on these two terms. As solar zenith angle increases, the solar beam at the surface level decreases, but the downward solar diffuse irradiance may increase in some situations. If the solar beam is included in the total solar irradiance incident on a surface and surface reflectance (also called as hemispherical reflectance or albedo in the visible and near-infrared range) is defined as the ratio of the total solar radiance reflected from the surface to the total solar irradiance, the surface reflectance will be dominated by the BRDF of the solar beam and therefore the reflectance depends on solar zenith angle significantly [31]. After the solar beam is separated from the total downward solar irradiance, we can use the BRDF anisotropic factor to calculate the surface-reflected solar beam and use the surface reflectance to calculate the surface-reflected solar downward irradiance. In this way, the solar angle and viewing angle dependences in the surface reflectance will be smaller so that we can assume the surface as a Lambertian surface.

Based on above assumptions, we have developed the following physics-based day/night LST model from (1). The radiance measured in MODIS band j can be expressed as

$$L(j) = t_1(j) \epsilon(j) B_j(T_s) + L_a(j) + L_s(j) + \frac{1 - \epsilon(j)}{\pi} [t_2(j) \alpha \mu_0 E_0(j) + t_3(j) E_d(j) + t_4(j) E_t(j)], \quad (3)$$

where all terms are band-averaged, $\epsilon(j)$ is the band emissivity which will be given in (5), similarly for $B_j(T_s)$, $L_a(j)$, $L_s(j)$, and $E_0(j)$. $E_d(j)$ and $E_t(j)$ are the band-averaged solar diffuse irradiance and atmospheric downward thermal irradiance at surface. And $t_i(j)$, $i = 1, \dots, 4$ are the band effective transmission functions weighted by the band response function and the corresponding radiance and

irradiance terms. Note that we have neglected the in-band spectral variation of the surface emissivity in reducing (1) into (3), and omitted symbols of view angle and solar angle for most terms in the above equation. On the right-hand side of this equation, $\epsilon(j)$, α , and $B_j(T_s)$ depend on surface properties and conditions, all other terms depend on atmospheric water vapor and temperature profiles, solar angle and viewing angle. These terms can be given by numerical simulations of atmospheric radiative transfer. The spectral response functions measured from the Engineering Model of the MODIS instrument have been used as weights in calculations of band averages of these terms.

If we use 2 measurements (day and night) in N MODIS TIR bands, we have $2N$ observations. The number of unknown variables are N band emissivities, daytime surface temperature T_{s-day} , nighttime surface temperature $T_{s-night}$, 4 atmospheric variables (T_a and cwv at two times), and the anisotropic factor α , totalling $N + 7$. The number of observations must be equal to or larger than the number of unknowns,

$$2N \geq N + 7 \quad . \quad (4)$$

So $N \geq 7$. Note that it is necessary to apply independent shapes of atmospheric temperature and water vapor profiles for daytime and nighttime so that temporal variations and temperature inversion (more often at night) could be considered in the LST retrieval. For the MODIS LST algorithm, these 7 bands are MODIS bands 20, 22, 23, 29, 31-33. According to the experience from the Engineering Model of the MODIS instrument, the NE Δ T in band 33 may be reduced from 0.25 °K to 0.12 °K, and it appears possible to achieve the goal for absolute calibration accuracy, 0.5-0.75%, for these 7 TIR bands. It seems that we can find unique solutions for the above 14 unknowns using 14 observations. But it is actually not true because: 1) the atmospheric profile is a continuous function of height and there are only a finite number of MODIS sounding bands so that the atmospheric temperature and water vapor profiles can be retrieved only at a finite number of levels, 2) there are always uncertainties in the retrieved atmospheric profiles and even in their shapes, 3) there are always instrument noises in the measurement data, 4) there are uncertainties in the atmospheric optical properties including water vapor absorption coefficients which we used in the development of LST algorithms. Therefore all we can do is to use a best combination of available bands and use an appropriate method to find the best estimates

of the unknown variables. We also need to use enough a priori knowledge and constraints of the atmosphere and the surface as "virtual measurements" to make the retrieval problem well posed [32]. The advantage of using daytime data in MODIS bands 20 and 22-23 is that solar radiation can be used as TIR source in the medium wavelength range so that the day/night LST model is essentially an active method to get the information of surface reflectance. Combining with the nighttime data in these 3 bands and day/night data in other 4 MODIS bands makes it possible to simultaneously retrieve surface emissivity and temperature. The advantage of including 4 atmospheric variables (T_a and cwv in daytime and nighttime) is that they can in part absorb errors caused by these uncertainties so that surface emissivity and temperature can be retrieved at better accuracies.

B. Band-Averaged Emissivities of Land-Surface Materials

The band-averaged emissivity is defined as

$$\epsilon(j) = \frac{\int_{\lambda_{j,L}}^{\lambda_{j,U}} \Psi(\lambda) \epsilon(\lambda) d\lambda}{\int_{\lambda_{j,L}}^{\lambda_{j,U}} \Psi(\lambda) d\lambda} \quad (5)$$

where $\Psi(\lambda)$ is the spectral response function of band j , $\lambda_{j,L}$ and $\lambda_{j,U}$ are its lower and upper boundaries. By using MODIS spectral response functions, band-averaged emissivities can be calculated from published spectral reflectance data of 80 pure terrestrial materials [33, 28]. This spectral data base includes igneous, metamorphic, and sedimentary rocks, varnished rock surfaces, lichen-covered sandstone, soil samples, green foliage, senescent foliage, ice, and water surfaces with suspended quartz sediment and oil slicks. The sample names and numbers are listed in Table II. The calculated band emissivities in MODIS bands 20, 22, 23, 29, 31-33 are shown in Figure 2. The sample number corresponds to the sample name and the type of material in Table II. As shown in this figure, there are very strong variations in the band emissivities for rock and sand samples, and for some soil samples and senescent vegetation foliages. For example, the emissivity of sands in MODIS band 20 could be as low as 0.55. However, the band emissivities in MODIS bands 31-33 are larger than 0.8 for all samples in the spectral reflectance database. For water, ice, and green vegetation leaves, there are small emissivity

contrasts among these 7 bands and their band emissivities vary in small ranges.

C. Atmospheric Radiative Transfer Simulations

As well known, the accuracy of atmospheric radiative transfer numerical models depends on numerical methods to solve the radiative transfer equation and our knowledge of the atmosphere and its inherent optical properties [34]. There are many methods available to solve the atmospheric radiative transfer problem because their fundamental theory has proved to be mathematically interesting and because there are important applications in neutron diffusion theory, astrophysics, and earth sciences. For example, there are a variety of methods based on two-stream approximations [35, 36], 4-stream approximations [37], and others such as delta-M method [38], adding/doubling method [39], discrete ordinate method [40], and Monte Carlo simulation method [41]. We developed a radiative transfer model, which provides accurate matrix solutions of the azimuth-dependent scalar radiative transfer equation for a vertical inhomogeneous, multi-layer atmosphere using the adding/doubling method for the development of algorithms to estimate column ozone and LST in clear-sky conditions [42, 10, 17]. Results from this model match those from Stamnes and Conklin's discrete-ordinates [40] calculations to 4 decimal places. Atmospheric radiative models based on the adding/doubling method have advantages in easy implementation of surface interfaces, such as the air-water interface and interfaces for specular reflectance or BRDF reflectance, and in efficiently getting solutions for multiple boundary conditions.

The continuous update of the LOWTRAN code [24, 43] and MODTRAN code [25, 21] developed by the U.S. Air Force Geophysics Laboratory over the past two decades represents a significant progress in improving our knowledge of optical properties of the earth's atmosphere. A two-stream approximation with multiple scattering parameterization [43, 44] is used in the LOWTRAN model. The new versions of MODTRAN code have the option to use the discrete ordinate method.

In the TIR range, LOWTRAN7 [43] and MODTRAN [21] give transmission functions of each molecule at a wavenumber interval of 5cm^{-1} and 1cm^{-1} , respectively, based on degraded line-by-line spectra [45], which have been validated against laboratory measurements. Note that these transmission values are not monochromatic thus causing a violation of the Lambert-Bouguer-Beer law because of the complexity of molecular band absorption. This is true even for a narrow wavenumber interval of 1

cm^{-1} . One solution to this problem is to expand radiative transmission functions calculated from LOWTRAN or MODTRAN by using “exponential-sum fitting” [46]. Following this technique the monochromatic radiative transfer model [47] is applied separately to each term in the exponential-sum expansion, and the results are then summed. After convoluting these results with the spectral response function, we get band-averaged atmospheric terms in (3). Typically, the total number of the cross-product terms in the exponential-sum fitting formulation is over 1,000 so it is very computationally time consuming. The advantage in using the exponential-sum fitting formulation is that we can obtain more accurate results, for example, the resulted 3 effective transmission functions for the viewing path in (1) may be different by a few to several percents ($t_3 > t_1$ and $t_4 < t_1$) because of selective, wavelength-dependent molecular band absorption although these transmission functions are defined for a same optical path from the target to the top of the atmosphere in the viewing direction of the sensor. The correlated-k distribution method [48, 49] is an alternative to the exponential-sum-fitting method. Usually the number of terms used in the correlated k-distribution method is smaller so that it is computationally efficient and it gives quite accurate results. The multiple scattering algorithm in the MODTRAN code is being upgraded to include a “correlated-k” absorption characterization.

As shown in Fig. 1, the atmospheric transmission in the 8-13 μm window, where 3 MODIS bands are located for the purpose of remote measurements of surface temperature, strongly depends on water vapor absorption including band absorption and continuum absorption. A review for measurements of water vapor absorption in the 8-13 μm atmospheric window reveals a considerable variation in its magnitude over the past 20 years [50]. The accuracy of water vapor continuum absorption in five of the measurements reviewed is about 10%, adequate experimental measurements are lacking at temperatures below 280°K. There is no accepted theory for the continuum absorption. Recent theoretical studies [51, 52] on water vapor continuum absorption have led to significant progress in understanding the physical mechanisms and the temperature dependence of the continuum absorption. But it is still premature to theoretically determine the magnitude and the temperature dependence of the water vapor continuum absorption coefficients. Thus, modelers must rely on empirical formulations [53, 54] based on laboratory measurements [55]. Atmospheric conditions, especially cold temperatures and/or high humidities, are difficult if not impossible to reproduce in the laboratory. This is particularly

true in the vital area of continuum absorption. Studies at relative humidities over 70% are a persistent problem. This is the threshold for condensation on hygroscopic dust particles and therefore for fogging of optical elements. Furthermore, laboratory spectroscopists have reached an impasse in the area of line wings and the continuum that prevents progress in line-by-line modeling [56]. In the past several years, the water vapor absorption has been compared and validated with High-Resolution Interferometer Sounder (HIS) spectral radiance data involving vertical path measurements from an aircraft, as well as from the ground [57, 58], and long-path atmospheric transmission measurements [59]. The empirical continuum formulation used in the FASCODE code [45], as well as in LOWTRAN and MODTRAN codes has been changed several times in the past decade. In the LOWTRAN7 code [43] and earlier versions of the MODTRAN code [25], the magnitude of the water vapor self continuum absorption coefficient in the 8.5-13 μm window is smaller by about 20% compared to that used in the LOWTRAN6 code [24]. Clough [60] made a new correction to the the water vapor continuum based on the measurement of the downwelling radiance at Kavieng, New Guinea by Westwater et al. [61] and the measurements by Revercomb and colleagues at the University of Wisconsin. This new continuum formulation has been implemented in version 3 of the MODTRAN code in 1994. Because the uncertainty in the water vapor continuum absorption coefficients may be larger than a few percents, it is not critical to neglect the small differences between transmission functions t_1 , t_3 and t_4 in (1) before the accuracy of the water vapor continuum absorption coefficients is significantly improved. So we make the same approximations $t_3 = t_1$ and $t_4 = t_1$ in (1) as made in the MODTRAN3 code up to its version 1.3 and in other models. The effect of these approximations should be considered along with uncertainties due to other sources when actual data are used to retrieve surface emissivity and temperature. Note that even we assumed that in each narrow spectral interval of 1 cm^{-1} or 5 cm^{-1} the transmission functions for the viewing path are equal in (1), the band effective transmission functions $t_3(j)$ and $t_4(j)$ may still be different from $t_1(j)$ in (3). Keeping in mind all the problems raised above for radiative transfer models, in this study we use version 1.3 of the MODTRAN3 code [21] to calculate all atmospheric and solar terms in (3). The discrete ordinate option with 8 streams is used in MODTRAN3 calculations so that the effect of multiple scattering due to background aerosols is considered in the calculations of the path radiances and the downwelling irradiances.

The path radiance resulting from scattering of the solar radiation in (3), $L_s(j)$, does depend on the relative azimuth between viewing direction and the solar beam direction. This dependence is determined by the aerosol loading, its size distribution, type and scattering phase function. These aerosol information and properties are not readily available in most situations. As shown in Fig. 1, the total aerosol effect on the transmission function in the thermal infrared range is small in normal clear-sky conditions. Radiative transfer simulations indicate that the value of L_s is only several hundredths of the direct solar beam value at the surface level, and that the azimuth dependence in L_s is less than 10%. So it is appropriate to neglect this azimuth dependence and to use the azimuth-averaged value of L_s in the new LST algorithm.

D. Variations of Atmospheric Conditions

It is important that a practical LST algorithm should accommodate atmospheric variations in a range that is wide enough to cover all possible real situations. For LST retrieval, we only consider atmospheric variations in clear-sky conditions. In the thermal infrared range, the most important atmospheric variables are atmospheric water vapor and atmospheric temperature profiles. Atmospheric absorption and thermal emission occur mainly in the lower troposphere. Radiative transfer simulations show that the effect of changing atmospheric water vapor and temperature profiles at elevation levels above 9km is almost negligible. We assume that the MODIS product of the atmospheric temperature and water vapor profiles retrieved from MODIS sounding channel gives the shapes of the profiles better than their absolute values because of the difficulties in decoupling the atmosphere-land interaction. Atmospheric temperature and water vapor at any level will be interpolated from their values retrieved at fixed levels. Given the shapes of temperature and water vapor profiles, we can use only two variables to describe variations of the clear-sky atmospheric condition: a shift of the temperature profile below elevation 9km, and a scaling factor for the water vapor profile. The column water vapor can be determined by the shape and the scaling factor. In order to build a data base for the atmospheric and solar terms in (3), we will select two dozens of basic atmospheric profiles considering different shapes of temperature and water vapor profiles, and the range of air surface temperatures in different regions and seasons. Some basic atmospheric profiles include temperature inversion layers. Then we add more variations to each of these basic atmospheric profiles in the following ways: 1) To add δT to the

atmospheric temperature profile at all levels between surface and elevation 9km, δT varies from -10°K to $+20^\circ\text{K}$ in steps of 2°K . The modified atmospheric temperature at the surface level, T_a , will be used as representative of the entire atmospheric temperature profile. 2) To scale the atmospheric water vapor profile at all levels between surface and elevation 9km in steps of 10% so that the column water vapor varies from 10% to 120% of the basic value.

E. Variations of the Land-Surface Temperature

In the simulation study of the new LST algorithm, we consider LST variations in a wide of range. The daytime surface temperature varies from atmospheric surface temperature T_{a-day} to $T_{a-day} + 24^\circ\text{K}$ in steps of 6°K , and the nighttime surface temperature varies from $T_{a-night} - 13.5^\circ\text{K}$ to $T_{a-night} + 4.5^\circ\text{K}$ in steps of 4.5°K .

III. NUMERICAL METHODS USED IN THE NEW LST ALGORITHM

A. Look-Up Table Method

In order to save computational time on numerical simulations of atmospheric radiative transfer for calculating the atmospheric and solar terms in (3), look-up tables will be used in the new LST algorithm. In this way, we only need to make a complete series of radiative transfer simulations once to build these look-up tables. Because multi-dimension interpolations are involved in our look-up table method, linear interpolation is most efficient. This requires smaller intervals (or steps) for these look-up tables. For example, the step for the atmospheric temperature variation is 2°K , the step for atmospheric column water vapor is 10% of the average value, the step for solar zenith angle and viewing zenith angle is 10° for angles smaller than 30° and 5° for larger angles. The upper limits for solar and viewing zenith angles are 75° and 65° , respectively. Similarly, a look-up table in a step of 0.1°K is also built for the band-averaged Planck functions in the temperature range $200\text{--}400^\circ\text{K}$. It is required that errors due to look-up tables and interpolation methods should be smaller than $\text{NE}\Delta T$. If this resolution scheme is used to build a look-up table for the 3 solar terms in (3) for about 24 basic atmospheric profiles, the total size of the look-up table is about 20MB. If using less space for look-up tables is a higher priority of considerations, we can use 3-point interpolation method so that 6 zenith

angles are enough for viewing and solar angles. However, 3-point interpolation takes much more computational time than linear interpolation. The size of look-up tables for other 3 atmospheric terms (transmission, thermal infrared path radiance, and downward thermal infrared irradiance) is much smaller.

B. Approaches to Solve the Retrieval Problem

We have developed two approaches to solve the LST retrieval problem. The first one is using statistical regression method, and the second one is using other numerical methods to solve the set of nonlinear equations (3).

In a linear approximation of equation (3) in the proximities of reference values of surface temperature and band emissivities, the left-hand side reduces to the band brightness temperature and the right-hand side reduces to surface temperature and band emissivities. Combining 14 equations together, the solution for surface temperature and band emissivities should be a linear combination of the band brightness temperatures, each of which corresponds to one of the 14 observations. Its mathematical form is

$$x_i = \sum_{j=1}^{14} w_{i,j} y_j + w_{i,0} , \quad (6)$$

where x is a vector of the 14 variables including surface temperatures and band emissivities, y_j is the band brightness temperature for observation j , and $w_{i,j}$, $i = 1, \dots, 14$ and $j = 1, \dots, 14$ are coefficients. And $w_{i,0}$ is the coefficient for the offset term. We can find these coefficients in two steps. In step 1, we construct a large sets of simulated observation values in wide ranges of atmospheric and surface conditions. In step 2, we make a statistical regression analysis using the band brightness temperatures associated with these simulated band radiance values as independent variables and using the given surface band emissivities and temperatures, and atmospheric parameters as dependent variables. The output of this regression analysis will be the coefficients in (6). The process of statistical regression analysis takes a lot of computational time. But it needs only to be done once. The values of x_i provided by this approach are the best estimates of these unknown variables in the statistical sense.

If we have better information on the shapes of the atmospheric temperature and water vapor profiles for the time which makes it possible to have a clear-sky day/night pairs of MODIS data, we can use other methods to numerically solve the set of nonlinear equations (3). We tried the Quasi-Newton method [62] and the Least-Squares Fit (χ^2 fit) method [63]. As Rodgers [32] pointed out, retrieval problem in remote sensing is generally nonlinear. The main sources of the nonlinearity in (3) are: 1) temperature dependence of the atmospheric transmission, 2) the dependence of transmission on absorber concentration, 3) temperature dependence of the Planck function, 4) wavelength dependence of the Planck function across a spectral band, 5) wavelength dependence of the Planck function between spectral bands, and 6) nonlinear constraints.

The initial values of the 14 unknown variables are given in their constrained ranges based on reasonable guesses or statistical analysis. The Quasi-Newton method is slightly more computationally efficient. These two methods give similar results in cases not including noise. It is well known [63, 62] that global convergence to right solutions is not guaranteed for nonlinear problems, especially when noise is included. The χ^2 fit method is selected in the new LST algorithm because it is more stable in our simulation studies. We are only interested in real situations where there is noise in remote measured data due to the intrinsic instrument noise and the turbulence in the atmosphere.

A measure of the goodness of χ^2 fit is defined by [63]

$$\chi^2 = \sum_{j=1}^{14} \left(\frac{1}{\sigma_j^2} [L_j - L(j)]^2 \right), \quad (7)$$

where L_j is the scaled band radiance observation value, $j = 1, 7$ for daytime, $j = 8, 14$ for nighttime. $L(j)$ is the scaled band radiance function in (3), which depends on unknowns x_i , $i = 1, 14$. We use the values of band-averaged Planck functions at a reference temperature, 300 °K, to scale the band radiance in corresponding bands so that the scaled differential radiance may be comparable. The term σ_j is the uncertainty in observation value L_j . In cases without noise, σ_j is identically equate to 1. However, for cases which include noise NEAT, σ_j will be

$$\sigma_j = L_j \frac{n_j \Delta T_{neq}(j)}{T_b(j)} \quad (8)$$

based on the following approximation for the band-averaged Planck function

$$L_j \approx C_j T_b^{n_j}(j) \quad (9)$$

where $\Delta T_{neq}(j)$ is the NE Δ T value in band j , and $T_b(j)$ is the brightness temperature corresponding to band radiance L_j . In the temperature range 240-400 °K, regression analysis gives the best fitting values for n_j , they are 12.91, 12.25, 11.98, 6.00, 4.70, 4.11, and 3.74 for MODIS bands 20, 22, 23, 29, 31-33. Note that this approximation is used only in calculation of σ_j , which determines the weight in (7). The effect of errors due to this approximation on solutions is negligible.

One of the difficulties in the χ^2 fit processing is that there may be more than one local minimum for χ^2 within a reasonable range of values for variable x_i , particularly in cases including noise. Therefore the final solution may depend on their initial values. We use two different ways to make the initialization. In the first way, we use a dozen sets of initial values that are spread over preassigned ranges all from minimums to maximums to get different solutions and select the solution associated with the minimum χ^2 value. In noisy situations, this selected solution may not be the best one we searched for. An alternative way is to use the estimates provided by the statistical regression method as the initial values. We use the second way in our LST algorithm. Typically, the χ^2 fit method takes 3-4 iterations to reach the final solution.

IV. SENSITIVITY AND ERROR ANALYSIS

Using look-up tables, we can quickly construct 14 band radiance values (7 values for daytime and other 7 values for nighttime) at the top of the atmosphere for any given conditions of surface band emissivities and BRDF anisotropic factor, daytime and nighttime surface temperatures, daytime and nighttime atmospheric surface temperatures and column water vapor values, solar angle and viewing angle. Then we can use these 14 radiance values as simulated MODIS observations to retrieve the given surface and atmospheric variables. We can then construct a sensitivity and error analysis,

presented in the following sub-sections.

A. Errors Due to Look-up Table and Interpolation Methods

In the first numerical simulation experiment, we do not include any noise in the data construction in order to test the numerical method to solve the nonlinear problem and to evaluate the errors due to using look-up tables and interpolation methods. We use the temperature and water vapor shapes in the “standard” mid-latitude summer atmospheric profiles and set the daytime and nighttime atmospheric surface temperatures at 298.2 °K and 290.2 °K. The column water vapor is set at 2.6cm for both daytime and nighttime for simplicity. In real applications, we use independent variables for the column water vapor in daytime and nighttime. We set anisotropic factor as 1, solar zenith angle at 45 °, viewing angle at nadir for daytime and nighttime, 5 different daytime surface temperatures ranging from 298.2 °K to 322.2 °K, and 5 different nighttime surface temperatures ranging from 276.7 °K to 294.7 °K. There are 25 cases of different daytime and nighttime surface temperatures for each sample of 80 surface materials. The band emissivities of these 80 terrestrial material samples cover the range from 0.55 to almost unity. The standard deviations of errors in retrieved surface temperatures are 0.27 and 0.21 °K for daytime and nighttime, the standard deviations of errors in retrieved emissivities are in 0.005-0.008 for bands 1 to 6, and 0.012 for the last band because of the low transmission of MODIS band 33 in the atmospheric condition. The standard deviations of errors in retrieved BRDF anisotropic factor, atmospheric temperatures, and column water vapor are 0.08, 0.10-0.15 °K, and 0.06cm, respectively. These numbers indicate that look-up tables are appropriate and the χ^2 fit method works well.

B. Sensitivities to the Uncertainties in Atmospheric Profile Shapes

In the second simulation experiment, we set the NEAT values for the 7 bands at 0.05, 0.07, 0.07, 0.05, 0.05, 0.05, and 0.12 °K, set 0.5% as the systematic calibration error for all bands, and keep all other parameters as in the first experiment. In our simulation, NEAT is treated as a random noise. We consider 4 different atmospheric conditions in mid-latitude summer, one of them is the “standard” condition used in MODTRAN code (“standard” means averaged here). As shown in Fig. 3, three of them have almost the same air temperature at the surface level, but they have very different shapes in

the temperature and water vapor profiles. The temperature profile in the last condition, labeled by “standard-4K”, is the “standard” temperature profile shifted by -4°K . Its water vapor profile is as same as in the “standard” profile in mid-latitude summer. The temperature discrepancy between the standard profile and profile A109 may be as large as 10°K at elevations near 2km and between 6-10km. The difference in water vapor profiles in atmospheric conditions of “standard”, A109, and A115 may be 20% to 50% or more. We established separate data bases of the atmospheric terms in (3) through atmospheric radiative transfer simulations for these different atmospheric conditions. The separate data bases will be used to calculate the daytime and nighttime band radiances in 7 MODIS bands in wide ranges of surface temperature for 80 surface samples. These calculated band radiances are then used as simulated observations. The coefficients in (6) were obtained by statistical regression analysis on the observations simulated for the standard atmospheric condition. We suppose that there is enough information available for the standard atmospheric condition, but there is no information available on the shapes of the atmospheric profile for atmospheric conditions A109 and A115. In the statistical approach, we apply the same set of regression coefficients to the 4 sets of simulated observations data for retrieving surface temperatures and emissivities. In the χ^2 fit approach, these surface temperatures and band emissivities retrieved by the regression approach are used as initial values for further iterative processing. The standard deviations of errors in surface temperatures and band emissivities retrieved by the statistical regression method are given in the first part of Table III, and those retrieved by using the χ^2 fit method are given in the second part. Comparing the results from the statistical approach and χ^2 fit approach for the standard atmospheric condition indicated that the χ^2 fit method gives significant improvements on retrieved surface temperatures and band emissivities. This is because we know the shapes of the atmospheric temperature and water vapor profiles well enough so that we can select the right set of the regression coefficient and the right parts from the look-up tables for the atmospheric and solar terms in (3). But for atmospheric conditions A109 and A115, we do not have the information for making these right selections. So the results retrieved from the χ^2 fit approach are worse than those from the statistical approach. However, for the case with the shifted “standard” temperature profile, the standard deviations of errors in surface temperatures retrieved by using the χ^2 approach is reduced by a factor of 2, and the accuracies of retrieved band emissivities are improved by about 50% because the shapes of atmospheric temperature and water vapor profiles in this case are as same as those in the

standard profiles. From this experiment we gained the following insights: the statistical method is less accurate but is also less sensitive to uncertainties in the atmospheric profile shapes; and the χ^2 fit method may be more accurate but it is more sensitive to uncertainties in the profile shapes. In the following part of this paper, we assume that the information of the profile shapes is available so that it is appropriate to pursue the χ^2 fit approach.

C. Sensitivities to the Three Assumptions of Surface Optical Properties

In the first test, C1, of the third simulation experiment, we set the NEAT values for the 7 bands at 0.05, 0.07, 0.07, 0.05, 0.05, 0.05, and 0.12 °K, set 0.5% as the systematic calibration error for all bands, and keep all other parameters as in the first experiment. The errors in surface temperatures retrieved by the χ^2 fit method for a total of 2,000 different cases are shown in Fig. 4A. The errors in retrieved band emissivities in MODIS bands 31 and 32 are shown in Fig. 4B. The standard deviations of errors in retrieved surface daytime and nighttime temperatures are in range of 0.4-0.5 °K, and the standard deviations of errors in band-averaged emissivities in MODIS bands 31 and 32 are 0.009 over a wide range of surface temperatures in the mid-latitude summer atmospheric condition. We can see the effect of the 0.5% systematic calibration error in Fig. 4A. This forces the retrieved temperature to shift to the positive direction by about 0.2 °K. The histograms of errors in retrieved surface temperatures and emissivities in bands 31 and 32 for a total of 2,000 cases are shown in Fig. 5A and 5B. We also applied the day/night LST method to “sample” mixed with two samples of the 80 terrestrial materials at different surface temperatures. Similar results have been obtained as long as band emissivities of the mixed sample are calculated from the components with their proportions as weights and its effective surface temperature is calculated from the total thermal radiation in MODIS band 31. The effective surface temperature of a mixed pixel does depend on band number, but this dependence is very small (at the instrument noise level) in normal surface conditions. We do not consider forest fires in the LST processing because the MODIS TIR bands may be easily saturated by subpixel fires at a small size and there is no sufficient knowledge on the optical properties of fires and smoke for making atmospheric corrections. In test C1 of this experiment, the maximum error in the retrieved LST is 3.2 °K for only one case (for the Indian grass sample at temperature 322.2 °K). Without considering this extreme case, the maximum error in retrieved LST will be 2.2 °K. Note that we simulated the surface temperature

variation in a very wide range. For each sample, the surface temperature varies in a range of 24 °K in daytime, and in a range of 18 °K in nighttime. These ranges are too wide for some land covers in real situations. For example, the temperature of snow cover and ice could not be above a few degrees C even considering possibly some small proportion of other land covers mixed in the scene, and the temperature of water surface and green vegetation leaves is not likely to be warmer than the surface air temperature by 24 °K. In favorable conditions (for example, higher solar elevation and surface temperature being in a normal range are favorable conditions for land covers with low reflectances), the solar beam can be effectively used as an active TIR source for remote measurements of the surface reflectance so that the band emissivities in MODIS bands 31 and 32 can be retrieved at an accuracy better than 0.01. Then these retrieved emissivities can be used in the generalized split-window LST algorithm [17] to quickly retrieve LST in the same area for a period of one or more weeks depending on season and weather conditions.

Now we check whether it is possible to relax the three assumptions of surface optical properties made in section II.A. The first row in Table IV gives standard deviations of the surface temperature and emissivities retrieved in test C1 of this experiment. In tests C2 and C3, we introduce some variations for the nighttime surface band emissivities to simulate its possible change with surface moisture content. In test C2, the nighttime band emissivities increase by 0.01 and they are only limited by its maximum value 1. In test C3, the emissivity increment depends on its value, a lower band emissivity could increase more. This may be the case for sands, its emissivity in MODIS band 20 is about 0.56, it could increase to 0.604 at night. The standard deviations of errors in daytime and nighttime surface temperatures, and band emissivities retrieved by the χ^2 fit method are increased slightly. Note that the retrieved emissivities are compared to daytime emissivities only. In tests C4 and C5, we set different BRDF anisotropic factors for the three bands in the mid-infrared range by differences of 5% and 10%. There is no significant change in the retrieved surface temperature and emissivities. In tests C6 and C7, we use non-Lambertian reflectance for the surface-reflected solar diffuse irradiance and atmospheric downward irradiance terms. They differ from the reflectance of a Lambertian surface by $\pm 20\%$. The effect of the non-Lambertian reflectance is also not significant. Comparing the standard deviations in tests C2 through C7 to those in test C1 shows that the maximum difference in standard deviations of

errors in retrieved surface temperatures is 0.17°K and the maximum difference in standard deviations of errors in retrieved band emissivities is 0.005, they are comparable to or smaller than the effects due to NEAT and calibration errors of the instrument. Therefore, we do not need to understand the three assumptions of surface optical properties described in section II.A as strict constraints to the new LST algorithm.

D. Sensitivities to NEAT and Calibration Errors

In the fourth simulation experiment, we keep the atmospheric and surface temperature parameters as in the first experiment, but change NEAT and calibration error values in a series of tests, as shown in Table V. The first column in the table indicates the test number. Seven NEAT values for 7 bands used in the new LST algorithm are listed in the second column block, and a systematic calibration error for all bands in the third column. Standard deviations (δT_s) and maximum errors (ΔT_s) of the retrieved daytime and nighttime surface temperatures are given in columns 4-7. The standard deviations of errors in retrieved emissivities for MODIS bands 31 and 32 are given in the last two columns. Comparison between test D1 and test D2 indicates that the effect due to a systematic calibration error of 0.5% is comparable to the effect of the given NEAT values. Test D3 indicates that doubling the NEAT values increases the standard deviation of retrieved daytime surface temperature by about 0.2°K . Comparing tests D4 and D5 to test D2 indicates that errors in retrieved surface temperatures and band emissivities become larger as the calibration error increases. In order to achieve the 1°K requirement for the LST accuracy and to retrieve band emissivities in MODIS bands 31 and 32 at an accuracy of the 0.01 level, the calibration error should be smaller than 1%. The new LST algorithm requires small NEAT (large signal-to-noise ratio) and a high consistent calibration accuracy for the 7 bands used. The split-window SST and LST algorithms also need these requirements for MODIS bands 31 and 32. However, the new LST algorithm needs these requirements over a much wider spectral range.

V. CONCLUSION

We developed a physics-based LST algorithm that retrieves surface band emissivities and temperatures from day/night pairs of MODIS data in 7 TIR bands. Look-up tables and linear

interpolation scheme are used in order to achieve high efficiency. The look-up tables for atmospheric transmission, path radiance, downward thermal irradiance, and solar diffuse irradiance are calculated with the MODTRAN3 code. The set of 14 nonlinear equations in the LST algorithm is solved with the statistical regression method and the least-squares fit method. The new day/night LST algorithm has been tested with simulated MODIS data in wide ranges of atmospheric and surface conditions. Comprehensive sensitivity and error analysis has been made to evaluate the performance of the new LST algorithm and its dependence on surface optical properties, the ranges of atmospheric conditions and surface temperatures, and on the noise-equivalent temperature difference and calibration accuracy specifications of the MODIS instrument. In cases with a systematic calibration error of 0.5%, the standard deviations of errors in retrieved surface daytime and nighttime temperatures fall between 0.4-0.5 °K over a wide range of surface temperatures for mid-latitude summer conditions. The standard deviations of errors in retrieved emissivities in bands 31 and 32 are 0.009, and the maximum error in retrieved surface temperatures falls between 2-3 °K. The new LST algorithm is being validated with daytime and evening MAS (MODIS Airborne Simulator) data, ground measurements data of the surface emissivity and temperature. We will focus on validation of the algorithm in our next paper.

ACKNOWLEDGEMENTS

This work was supported by EOS Program contract NAS5-31370 of the National Aeronautics and Space Administration. The authors wish to express their gratitude to the National Center of Scientific Researches of France (CNRS) for the support to Z.-L. Li, who visited Institute for Computational Earth System Science, University of California at Santa Barbara, in 1995. During his visit, the authors made a fruitful collaboration. The MODTRAN3 code, released by Phillips Laboratory, Department of the Air Force, has been used for atmospheric radiative transfer simulations in this research. The authors would also like to thank the reviewers for their detailed comments, which helped to improve the paper.

REFERENCES

- [1] H. Mannstein, "Surface energy budget, surface temperature and thermal inertia," in *Remote Sensing Applications in Meteorology and Climatology*, ed. R. A. Vaughan and D. Reidel, NATO ASI Ser. C: Math. Phys. Sci. Vol. 201, pp. 391-410, Dordrecht, Netherlands: A Reidel Publishing Co., 1987.
- [2] P. J. Sellers, F. G. Hall, G. Asrar, D. E. Strebel, and R. E. Murphy, "The first ISLSCP Field Experiment (FIFE)," *Bull. Amer. Meteorol. Soc.*, vol. 69, no. 1, pp. 22-27, 1988.
- [3] T. J. Schmugge and J. C. André, Ed., *Land Surface Evaporation: Measurements and Parameterization*, New York: Springer-Verlag, 1991.
- [4] S. W. Running, C. Justice, V. Salomonson, D. Hall, J. Barker, Y. Kaufman, A. Strahler, A. Huete, J.-P. Muller, V. Vanderbilt, Z. Wan, and P. Teillet, "Terrestrial remote sensing science and algorithms planned for EOS/MODIS," *Int. J. Remote Sens.*, vol. 15, no. 17, pp. 3587-3620, 1994.
- [5] A. B. Kahle, D. P. Madura, and J. M. Soha, "Middle infrared multispectral aircraft scanner data: analysis for geological applications," *Appl. Optics*, vol. 19, pp. 2279-2290, 1980.
- [6] A. B. Kahle, "Surface emittance, temperature, and thermal inertia derived from Thermal Infrared Multispectral Scanner (TIMS) data for Death Valley, California," *Geophysics*, vol. 52, no. 7, pp. 858-874, 1986.
- [7] S. J. Hook, A. R. Gabell, A. A. Green, and P. S. Kealy, "A comparison of techniques for extracting emissivity information from thermal infrared data for geological studies," *Remote Sens. Environ.*, vol. 42, pp. 123-135, 1992.
- [8] J. C. Price, "Land surface temperature measurements from the split window channels of the NOAA-7 AVHRR," *J. Geophys. Res.*, vol. 79, pp. 5039-5044, 1984.
- [9] F. Becker, "The impact of spectral emissivity on the measurement of land surface temperature from a satellite," *Int. J. Remote Sens.*, vol. 8, no. 10, pp. 1509-1522, 1987.
- [10] Z. Wan and J. Dozier, "Land-surface temperature measurement from space: physical principles and inverse modeling," *IEEE Trans. Geosci. Remote Sens.*, vol. 27, no. 3, pp. 268-278, 1989.
- [11] F. Becker and Z.-L. Li, "Toward a local split window method over land surface," *Int. J. Remote Sens.*, vol. 11, no. 3, pp. 369-393, 1990.
- [12] J. A. Sobrino, C. Coll, and V. Caselles, "Atmospheric corrections for land surface temperature using AVHRR channel 4 and 5," *Remote Sens. Environ.*, vol. 38, no. 1, pp. 19-34, 1991.
- [13] A. Vidal, "Atmospheric and emissivity correction of land surface temperature measured from satellite using ground measurements or satellite data," *Int. J. Remote Sens.*, vol. 12, no. 12, pp. 2449-2460, 1991.

- [14] Y. H. Kerr, J. P. Lagouarde, and J. Imbernon, "Accurate land surface temperature retrieval from AVHRR data with use of an improved split window algorithm," *Remote Sens. Environ.*, vol. 41, no. 2-3, pp. 197-209, 1992.
- [15] C. Otte and M. P. Stoll, "Effect of atmospheric absorption and surface emissivity on the determination of land temperature from infrared satellite data," *Int. J. Remote Sens.*, vol. 14, no. 10, pp. 2025-2037, 1993.
- [16] A. J. Prata, "Land surface temperatures derived from the advanced very high resolution radiometer and the along-track scanning radiometer 2. experimental results and validation of AVHRR algorithms," *J. Geophys. Res.*, vol. 99, no. D6, pp. 13025-13058, 1994.
- [17] Z. Wan and J. Dozier, "A generalized split-window algorithm for retrieving land-surface temperature measurement from space," *IEEE Trans. Geosci. Remote Sens.*, vol. 34, no. 4, pp. 892-905, 1996.
- [18] Z.-L. Li and F. Becker, "Feasibility of land surface temperature and emissivity determination from AVHRR data," *Remote Sens. Environ.*, vol. 43, pp. 67-85, 1993.
- [19] V. Salomonson, W. Barnes, P. Maymon, H. Montgomery, and H. Ostrow, "MODIS: advanced facility instrument for studies of the Earth as a system," *IEEE Trans. Geosci. Remote Sens.*, vol. 27, no. 2, pp. 145-153, 1989.
- [20] M. D. King, Y. J. Kaufman, W. P. Menzel, and D. Tanré, "Remote sensing of cloud, aerosol, and water vapor properties from the Moderate Resolution Imaging Spectrometer (MODIS)," *IEEE Trans. Geosci. Remote Sens.*, vol. 30, no. 1, pp. 2-27, 1992.
- [21] A. Berk, L. S. Bemstein, and D. C. Robertson, "MODTRAN: A moderate resolution model for LOWTRAN 7," Rep. GL-TR-89-0122, Burlington, MA: Spectral Sciences, Inc., 1989.
- [22] W. L. Smith, H. M. Woolf, and A. J. Schriener, "Simultaneous retrieval of surface and atmospheric parameters: a physical and analytically direct approach," in *Advances in Remote Sensing Retrieval Methods*, ed. A. Deepak, H. E. Fleming, and M. T. Chahine, pp. 221-232, Hampton, Va., USA: A. Deepak Publishing, 1985.
- [23] Z. Wan and J. Dozier, "Effects of the atmosphere and surface emissivity on the thermal infrared spectral signature measured from MODIS-N," *Proc. IGARSS '90*, pp. 189-192, 1990.
- [24] F. X. Kneizys, E. P. Shettle, W. O. Gallery, J. H. Chetwynd, L. W. Abreu, J. E. A. Selby, S. A. Clough, and R. W. Fenn, "Atmospheric Transmittance/Radiance: Computer Code LOWTRAN 6," Rep. AFGL-TR-83-0187 (NTIS AD A137796), Bedford, MA: Air Force Geophys. Lab., 1983.
- [25] A. Berk, L. S. Bemstein, and D. C. Robertson, "MODTRAN: A moderate resolution model for LOWTRAN," Rep. AFGL-TR-87-0220, Burlington, MA: Spectral Sciences, Inc., 1987.

- [26] W. M. Cornette, P. K. Acharya, D. C. Robertson, and G. P. Anderson, "Moderate spectral atmospheric radiance and transmittance code (MOSART)," Rep. R-057-94(11-30), La Jolla, CA: Photon Research Associates, Inc., 1994.
- [27] W. P. Menzel and J. F. W. Purdom, "Introducing GOES-I - the 1st of a new generation of geostationary operational environmental satellites," *Bull. Amer. Meteor. Soc.*, vol. 75, no. 5, pp. 757-781, 1994.
- [28] J. W. Salisbury and D. M. D'Aria, "Emissivity of terrestrial materials in the 3-5 μm atmospheric window," *Remote Sens. Environ.*, vol. 47, pp. 345-361, 1994.
- [29] W. Snyder and Z. Wan, "Surface temperature correction for active infrared reflectance measurements of natural materials," *Appl. Optics*, vol. 35, no. 13, pp. 2216-2220, 1996.
- [30] W. Snyder, Z. Wan, Y. Zhang, and Y.-Z. Feng, "Thermal infrared (3-14 μm) bidirectional reflectance measurements of sands and soils," *Remote Sens. Environ.*, submitted 1996.
- [31] C. B. Schaaf and A. H. Strahler, "Solar zenith angle effects on forest canopy hemispherical reflectances calculated with a geometric-optical bidirectional reflectance model," *IEEE Trans. Geosci. Remote Sens.*, vol. 31, no. 4, pp. 921-927, 1993.
- [32] C. D. Rodgers, "Retrieval of atmospheric temperature and composition from remote measurements of thermal radiation," *Rev. Geophys. and Space Phys.*, vol. 14, no. 4, pp. 609-624, 1976.
- [33] J. W. Salisbury and D. M. D'Aria, "Emissivity of terrestrial materials in the 8-14 μm atmospheric window," *Remote Sens. Environ.*, vol. 42, pp. 83-106, 1992.
- [34] R. M. Goody and Y. L. Yung, *Atmospheric Radiation*, New York: Oxford University Press, 1989.
- [35] W. E. Meador and W. R. Weaver, "Two-stream approximation to radiative transfer in planetary atmospheres: a unified description of existing methods and a new improvement," *J. Atmos. Sci.*, vol. 37, no. 3, pp. 630-643, 1980.
- [36] D. Tanré, C. Deroo, A. Deleffe, M. Herman, and J. J. Morcrette, "Description of a computer code to simulate the satellite signal in the solar spectrum: the 5S code," *Int. J. Remote Sens.*, vol. 11, no. 4, pp. 659-668, 1990.
- [37] C. N. Cuzzi, T. P. Ackerman, and L. C. Helmle, "The delta-four-stream approximation for radiative flux transfer," *J. Atmos. Sci.*, vol. 39, no. 4, pp. 917-925, 1982.
- [38] W. J. Wiscombe, "The delta-M method: rapid yet accurate radiative flux calculations for strong asymmetric phase functions," *J. Atmos. Sci.*, vol. 34, pp. 1408-1422, 1977.
- [39] W. J. Wiscombe, "Extension of the doubling method to inhomogeneous sources," *J. Quant. Spectros. Radiat. Transfer*, vol. 16, no. 6, pp. 477-486, 1976.

- [40] K. Stamnes and P. Conklin, "A new multi-layer discrete ordinate approach to radiative transfer in vertically inhomogeneous atmospheres," *J. Quant. Spectrosc. Radiat. Transfer*, vol. 31, pp. 273-282, 1984.
- [41] C. N. Adams and G. W. Kattawar, "Radiative transfer in spherical shell atmospheres I. Rayleigh scattering," *Icarus*, vol. 35, no. 1, pp. 139-151, 1978.
- [42] R. C. Smith, Z. Wan, and K. S. Baker, "Ozone depletion in Antarctica: modeling its effect on solar UV irradiance under clear-sky conditions," *J. Geophys. Res.*, vol. 97, no. C5, pp. 7383-7397, 1992.
- [43] F. X. Kneizys, E. P. Shettle, L. W. Abreu, J. H. Chetwynd, G. P. Anderson, W. O. Gallery, J. E. A. Selby, and S. A. Clough, "Users Guide to LOWTRAN 7," Rep. AFGL-TR-88-0177, Bedford, MA: Air Force Geophys. Lab., 1988.
- [44] R. G. Isaacs, W.-C. Wang, R. D. Worsham, and S. Goldberg, "Multiple scattering LOWTRAN and FASCOD models," *Appl. Optics*, vol. 26, pp. 1272-1281, 1987.
- [45] S. E. Clough, F. X. Kneizys, E. P. Shettle, and G. P. Anderson, "Atmospheric radiance and transmission: FASCOD2," in *Proc. of the Sixth Conference on Atmospheric Radiation, Williamsburg, VA*, pp. 141-144, Boston, MA: American Meteorological Society, 1986.
- [46] W. J. Wiscombe and J. W. Evans, "Exponential-sum fitting of radiative transmission functions," *J. Comput. Phys.*, vol. 24, no. 4, pp. 416-444, 1977.
- [47] S. Chandrasekhar, *Radiative Transfer*, New York: Dover Publications, 1960.
- [48] A. A. Lacis and V. Oinas, "A description of the correlated kappa-distribution method for modeling nongray gaseous absorption, thermal emission, and multiple scattering in vertically inhomogeneous atmospheres," *J. Geophys. Res.*, vol. 96, no. D5, pp. 9027-9063, 1991.
- [49] Q. Fu and K.-N. Liou, "On the correlated k-distribution method for radiative transfer in nonhomogeneous atmospheres," *J. Atmos. Sci.*, vol. 49, no. 22, pp. 2139-2156, 1992.
- [50] W. B. Grant, "Water vapor absorption coefficients in the 8-13- μ m spectral region: a critical review," *Appl. Optics*, vol. 29, no. 4, pp. 451-462, 1990.
- [51] Q. Ma and R. Tipping, "A far wing line shape theory and its application to the foreign-broadened water vapor continuum absorption .3," *J. Chem. Phys.*, vol. 97, pp. 818-828, 1992.
- [52] Q. Ma and R. Tipping, "The detailed balance requirement and general empirical formalisms for continuum absorption," *J. Quant. Spectrosc. Radiat. Transfer*, vol. 51, pp. 751-757, 1994.
- [53] R. Robert, J. Selby, and L. Biberman, "Infrared continuum absorption by atmospheric water vapor in the 8-12 micron window," *Appl. Optics*, vol. 15, pp. 2085-, 1976.

- [54] S. A. Clough, F. X. Kneizys, and R. W. Davies, "Line shape and the water vapor continuum," *Atmos. Res.*, vol. 23, pp. 229-241, 1989.
- [55] D. E. Burch and R. L. Alt, "Continuum absorption by H₂O in the 700-1200 cm⁻¹ and 2400-2800 cm⁻¹ windows," Rep. AFGL-TR-84-0128, Hanscom AFB, MA: Ford Aerospace and Communication Corporate, 1984.
- [56] P. Varanasi, "On the nature of the infrared spectrum of water vapor between 8 and 14 μ m," *J. Quant. Spectros. Radiat. Transfer*, vol. 40, no. 3, pp. 169-175, 1988.
- [57] S. A. Clough, R. D. Worsham, W. L. Smith, H. E. Revercomb, R. O. Knuteson, G. P. Anderson, M. L. Hoke, and F. X. Kneizys, "Validation of FASCODE calculations with HIS spectral radiance measurements," in *IRS '88: Current Problems in Atmospheric Radiation*, ed. J. Lenoble and J.-F. Geleyn, pp. 376-379, Hampton, Va., USA: A. Deepak Publishing, 1989.
- [58] W. L. Smith, H. E. Revercomb, H.-L. Huang, and R. O. Knuteson, "Vertical sounding capabilities with high spectral resolution atmospheric radiation measurements - a demonstration with the High resolution Interferometer Sounder (HIS)," in *High Spectral Resolution Infrared Remote Sensing for Earth's Weather and Climate Studies*, ed. A. Chedin, M. T. Chahine, and N. A. Scott, pp. 131-146, Berlin, Germany: Springer-Verlog, 1993.
- [59] J.-M. Thériault, P. L. Roney, D. St.-Germain, H. E. Revercomb, R. O. Knuteson, and W. L. Smith, "Analysis of the FASCODE model and its H₂O continuum based on long-path atmospheric transmission measurements in the 4.5-11.5 μ m region," *Appl. Optics*, vol. 33, no. 3, pp. 323-333, 1994.
- [60] S. A. Clough, "The water vapor continuum and its role in remote sensing," in *Proc. of Conference on Optical Remote Sensing of the Atmosphere, Salt Lake City, Utah*, pp. 76-78, 1995.
- [61] E. R. Westwater, J. B. Snider, J. H. Churnside, and J. A. Shaw, "Ground based microwave and infrared radiance observations during Probe," in *Proc. of the Eighth Conference on Atmospheric Radiation, AMS, Nashville, TN*, pp. 272-275, 1994.
- [62] J.E. Dennis, JR. and R. B. Schnabel, *Numerical Methods for Unconstrained Optimization and Nonlinear Equations*, New Jersey: Prentice-Hall, Inc., 1983.
- [63] P. R. Bevington, *Data Reduction and Error Analysis for the Physical Sciences*, New York: McGraw-Hill Book Company, 1969.

Figure and Table Captions

Fig. 1, Atmospheric transmission functions at view angle 45° in mid-latitude summer condition (column water vapor 2.9cm, visibility 23 km).

Fig. 2, Band-averaged emissivities of 80 terrestrial material samples in MODIS bands 20, 22, 23, 29, 31-33.

Fig. 3, Atmospheric temperature (A) and water vapor (B) profiles in mid-latitude summer.

Fig. 4, Errors in surface temperatures (A) and in surface emissivities (B) retrieved by the χ^2 fit method.

Fig. 5, Histograms of errors in surface temperatures (A) and in surface emissivities (B) retrieved by the χ^2 fit method.

Table I

Specifications of the EOS MODIS bands.

Table II

List of terrestrial material samples.

Table III

The standard deviations of errors in surface temperature and emissivities retrieved with two approaches of the day/night LST algorithm.

Table IV

The standard deviations of errors in surface temperature and emissivities retrieved with the χ^2 fit approach of the day/night LST algorithm in the sensitivity study on assumptions of surface optical properties in conditions of $NE\Delta T = 0.05\text{--}0.12^\circ\text{K}$, systematic calibration error = 0.5%, $cwv = 2.6\text{ cm}$, $\alpha = 1.0$, $T_{a\text{-day}} = 298.2^\circ\text{K}$, and $T_{a\text{-night}} = 290.2^\circ\text{K}$.

Table V

The dependence of standard deviations (δT_s) and maximum errors (ΔT_s) in surface emissivities and temperatures retrieved with the χ^2 fit approach of the day/night LST algorithm on $NE\Delta T$ and calibration errors.

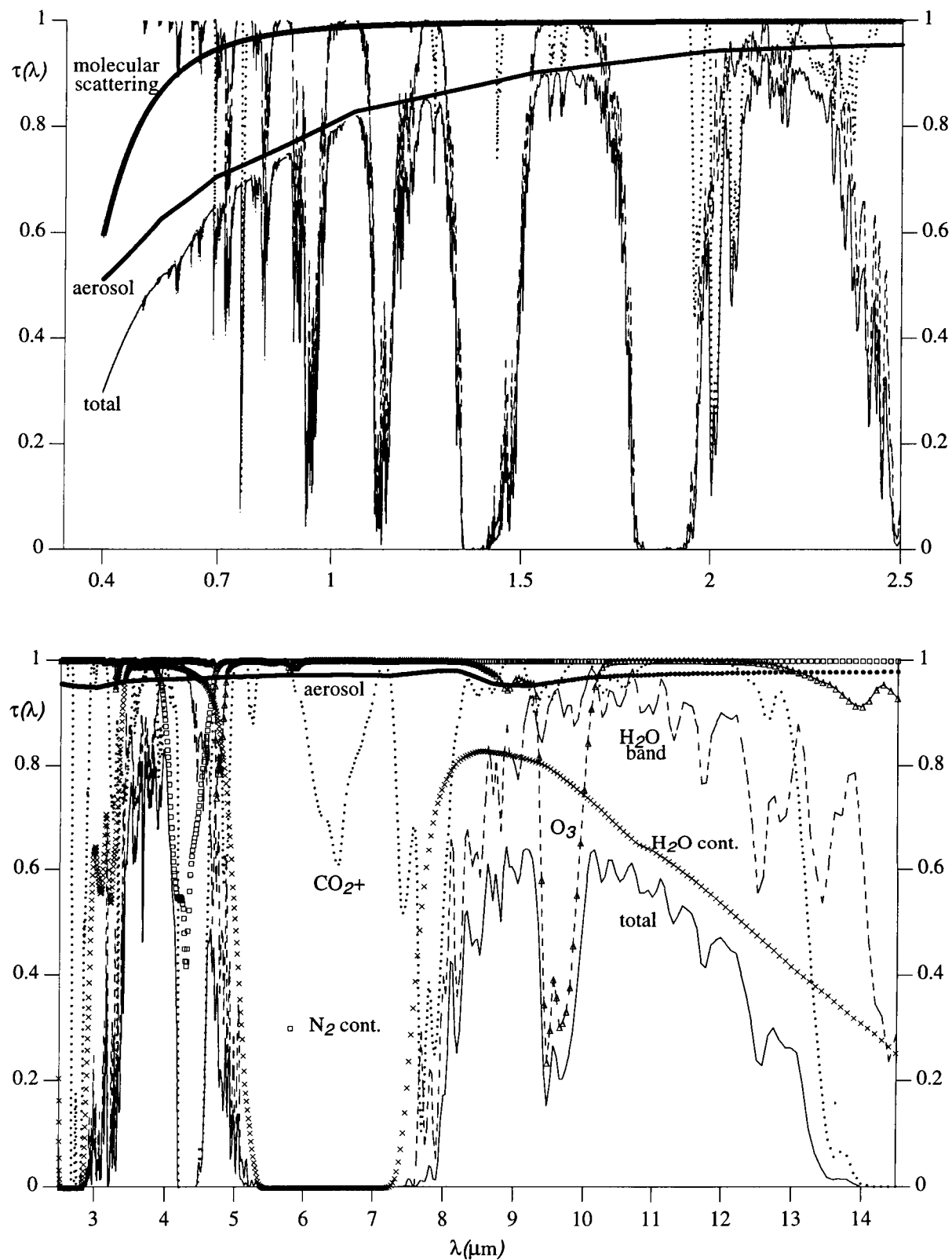


Fig. 1, Atmospheric transmissions at view angle 45° in mid-latitude summer condition (cwv = 2.9cm, vis. = 23km).

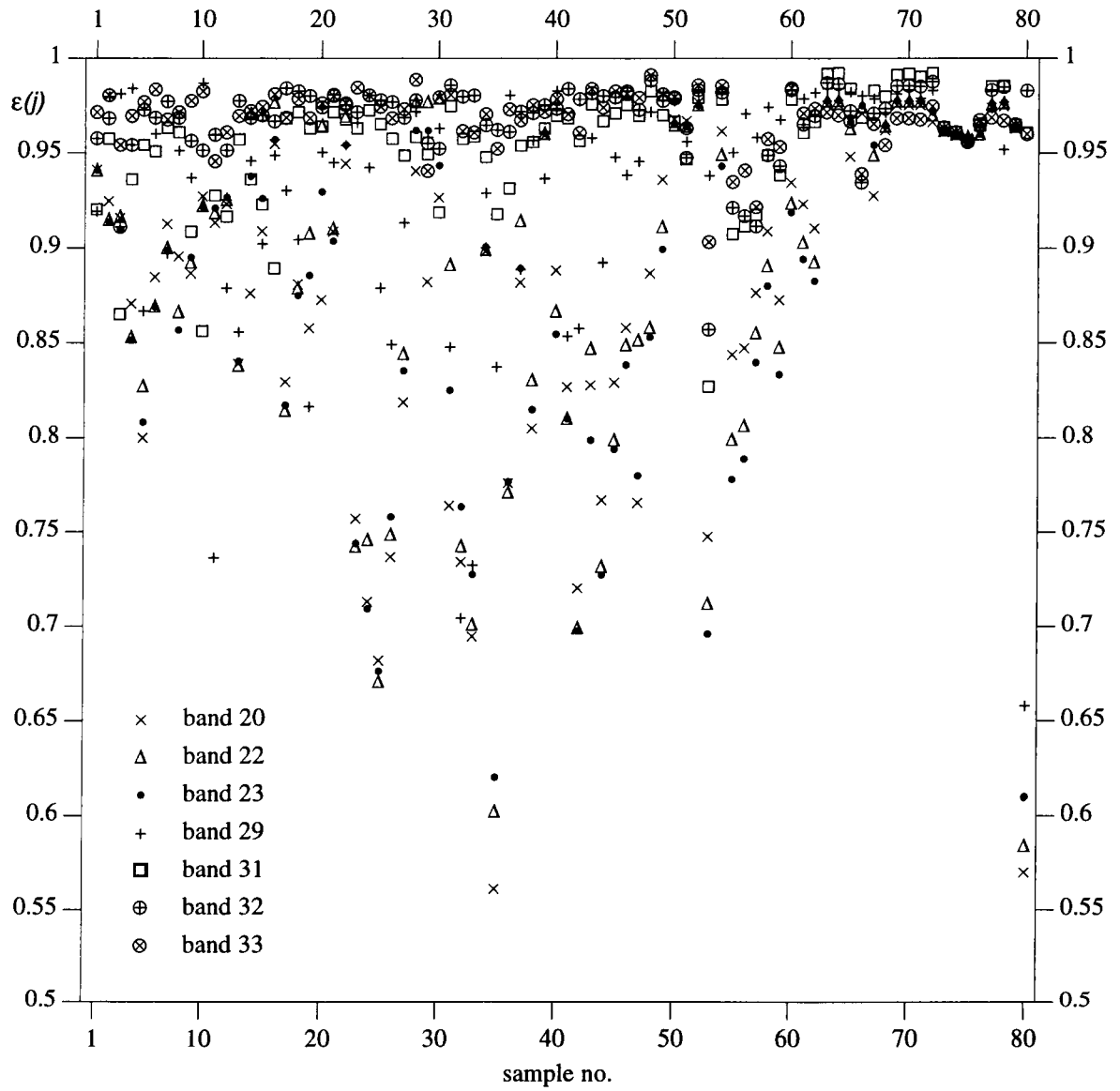


Fig. 2, Band-averaged emissivities in MODIS bands 20, 22, 23, 29, 31-33 versus samples in Table II.

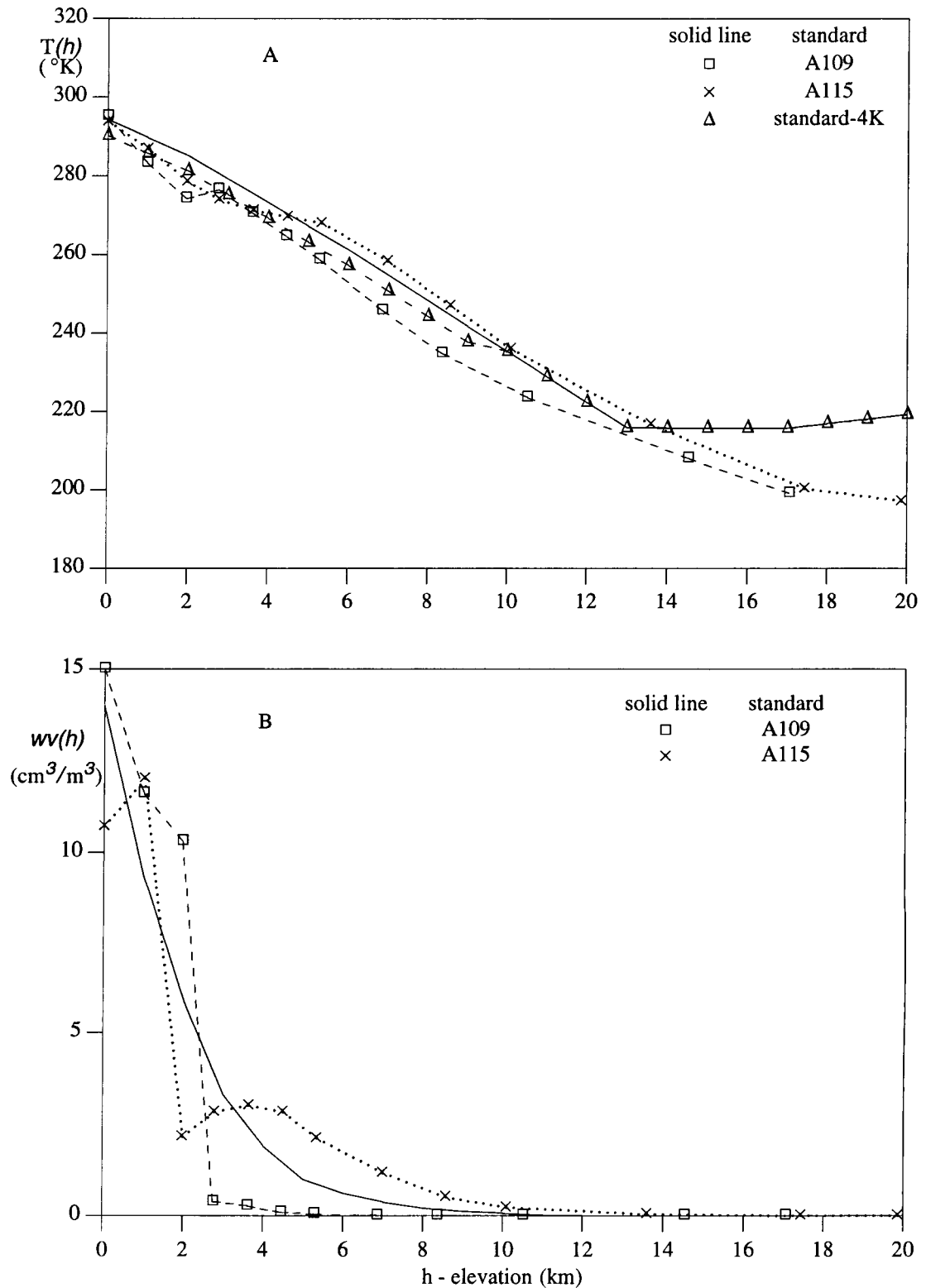


Fig. 3, Atmospheric temperature profiles (A) and water vapor profiles (B) in mid-latitude summer.

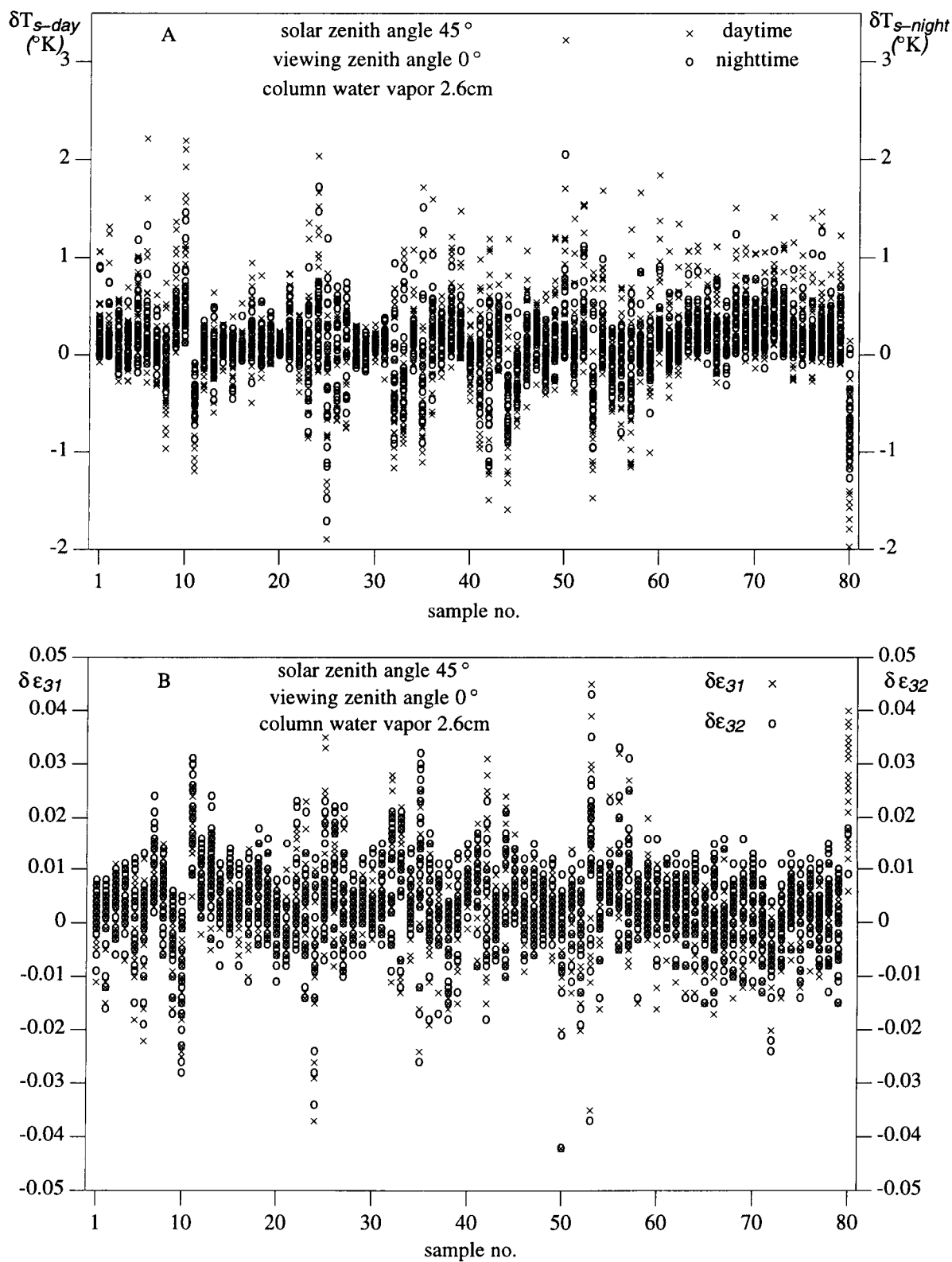


Fig. 4, Errors in surface temperatures (A) and emissivities (B) retrieved by the χ^2 fit method.

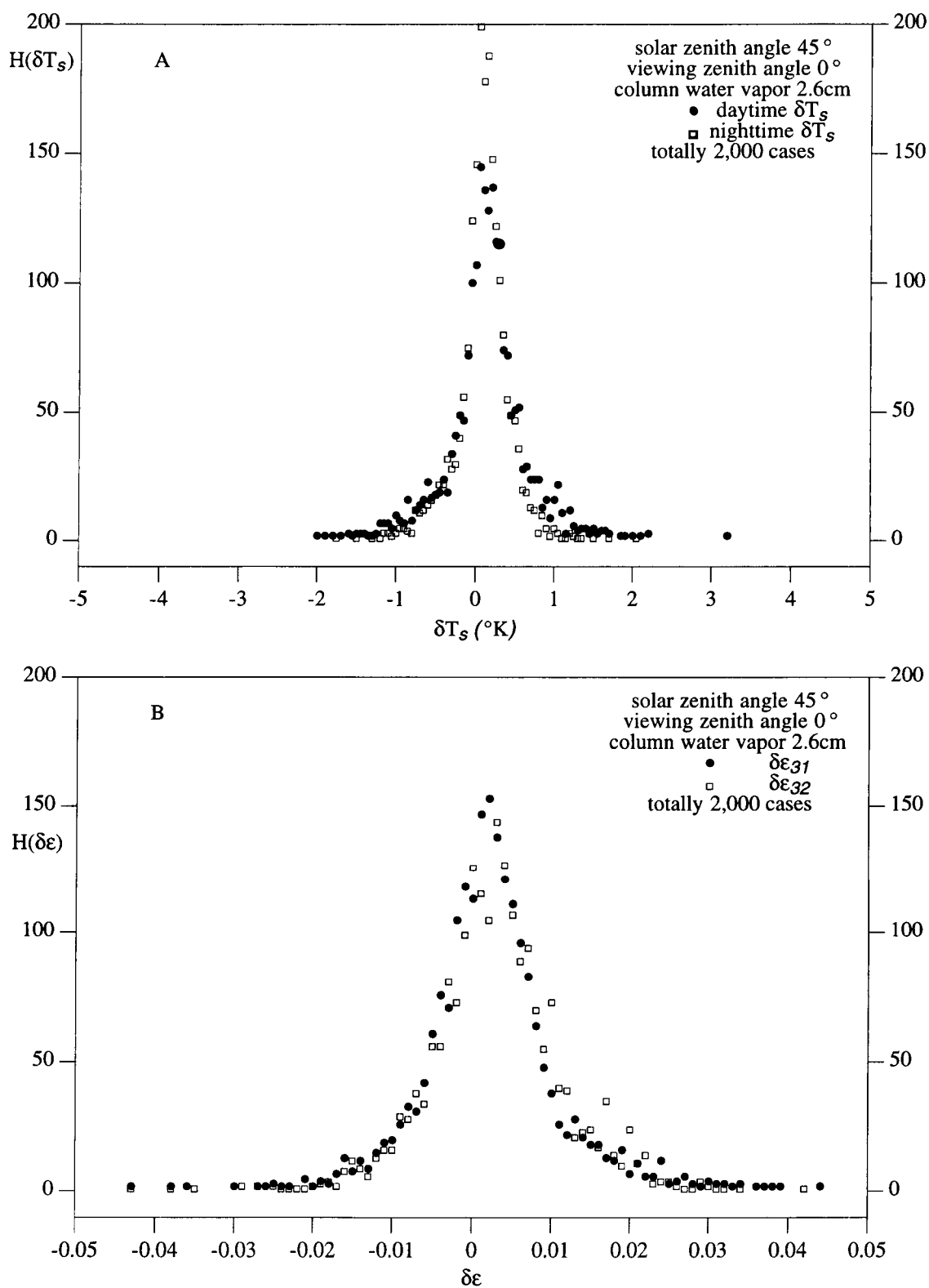


Fig. 5, Histogram of errors in surface temperatures (A) and emissivities (B) retrieved by the χ^2 fit method.

TABLE I. Specifications of the EOS MODIS bands.

| band | bandwidth (nm) | IFOV | primary use | band | bandwidth (μ m) | IFOV | $NE\Delta T$ ($^{\circ}$ K) | primary use |
|------|-------------------|------|----------------|------|-------------------------|------|---------------------------------|----------------|
| 1 | 620- 670 | 250m | L | 20 | 3.660-3.840 | 1km | 0.05 | O, L |
| 2 | 841- 876 | 250m | A, L | 21 | 3.929-3.989 | 1km | | fire, volcano |
| 3 | 459- 479 | 500m | L | 22 | 3.929-3.989 | 1km | 0.07 | A, L |
| 4 | 545- 565 | 500m | L | 23 | 4.020-4.080 | 1km | 0.07 | A, L |
| 5 | 1230-1250 | 500m | L | 24 | 4.433-4.498 | 1km | 0.25 | A |
| 6 | 1628-1652 | 500m | A, L | 25 | 4.482-4.549 | 1km | 0.25 | A |
| 7 | 2105-2155 | 500m | A, L | 27 | 6.535-6.895 | 1km | 0.25 | A |
| 8 | 405- 420 | 1km | O | 28 | 7.175-7.475 | 1km | 0.25 | A |
| 9 | 438- 448 | 1km | O | 29 | 8.400-8.700 | 1km | 0.05 | L |
| 10 | 483- 493 | 1km | O | 30 | 9.580-9.880 | 1km | 0.25 | ozone |
| 11 | 526- 536 | 1km | O | 31 | 10.780-11.280 | 1km | 0.05 | A, L |
| 12 | 546- 556 | 1km | O | 32 | 11.770-12.270 | 1km | 0.05 | A, L |
| 13 | 662- 672 | 1km | O | 33 | 13.185-13.485 | 1km | 0.25 | A, L |
| 14 | 673- 683 | 1km | O | 34 | 13.485-13.785 | 1km | 0.25 | A |
| 15 | 743- 753 | 1km | A | 35 | 13.785-14.085 | 1km | 0.25 | A |
| 16 | 862- 877 | 1km | A | 36 | 14.085-14.385 | 1km | 0.35 | A |
| 17 | 890- 920 | 1km | A | | | | | |
| 18 | 931- 941 | 1km | A | | | | | |
| 19 | 915- 965 | 1km | A | | | | | |
| 26 | 1360-1390 | 1km | cirrus | | | | | |

Note: A - atmospheric studies; L - land studies; O - ocean studies. Ref: MODIS Level 1B Algorithm Theoretical Basis Document, 1995, NASA/GSFC, Greenbelt, MD.

TABLE II. List of terrestrial material samples.

| sample no. | sample name | type of material | sample no. | sample name | type of material |
|------------|--------------|---------------------------|------------|---------------|-------------------------|
| 1 | basalt.f | desert vanish coated rock | 41 | 0135 | soil (Entisols) |
| 2 | basalt.v | desert vanish coated rock | 42 | 0145 | soil (Ultisols) |
| 3 | ijolite.f | desert vanish coated rock | 43 | 0211 | soil (Molisols) |
| 4 | ijolite.v | desert vanish coated rock | 44 | 0219 | soil (Alfisols) |
| 5 | rhyolite.f | desert vanish coated rock | 45 | 0226 | soil (Inceptisols) |
| 6 | rhyolite.v | desert vanish coated rock | 46 | 0475 | soil (Vertisols) |
| 7 | crustose.10 | lichens coated rock | 47 | 1530 | soil (Aridisols) |
| 8 | crustose.65 | lichens coated rock | 48 | 4717 | soil (Oxisols) |
| 9 | basalt.h7 | igneous rock | 49 | foliose.1 | veg., lichens |
| 10 | dunite.h1 | igneous rock | 50 | indiagr.ass | veg., green foliage |
| 11 | granite.h1 | igneous rock | 51 | redoak | veg., green foliage |
| 12 | syenite.h1 | igneous rock | 52 | white.ine | veg., green foliage |
| 13 | greywack.eh1 | sedimentary rock | 53 | senbeech | veg., senescent foliage |
| 14 | limeston.eh1 | sedimentary rock | 54 | senpine | veg., senescent foliage |
| 15 | limeston.eh2 | sedimentary rock | 55 | senredoa.kh1 | veg., senescent foliage |
| 16 | limeston.eh3 | sedimentary rock | 56 | senryegr.ass | veg., senescent foliage |
| 17 | sandton.eh1 | sedimentary rock | 57 | oakbark.1 | veg., tree bark |
| 18 | sandton.eh2 | sedimentary rock | 58 | pinebark.1 | veg., tree bark |
| 19 | sandton.eh4 | sedimentary rock | 59 | ypoplarb.ark | veg., senescent foliage |
| 20 | shale.h3 | sedimentary rock | 60 | conifer.ous | veg. decomposing litter |
| 21 | shale.h5 | sedimentary rock | 61 | decidu.ous | veg. decomposing litter |
| 22 | shale.h6 | sedimentary rock | 62 | wood | veg. decomposing litter |
| 23 | siltston.eh1 | sedimentary rock | 63 | seawater | water |
| 24 | siltston.eh2 | sedimentary rock | 64 | distwa.ter | water |
| 25 | gneiss.h1a | metamorphic rock | 65 | distice1.00g | ice |
| 26 | gneiss.h3a | metamorphic rock | 66 | distices.moo | ice |
| 27 | gneiss.h4 | metamorphic rock | 67 | seaice.10.ogr | ice |
| 28 | marble.h2 | metamorphic rock | 68 | seaicesm.oot | ice |
| 29 | marble.h3 | metamorphic rock | 69 | qtzwater.23 | suspended sediments |
| 30 | marble.h4 | metamorphic rock | 70 | qtzwater.64 | suspended sediments |
| 31 | quartzit.eh1 | metamorphic rock | 71 | qtzwater.7 | suspended sediments |
| 32 | quartzit.eh4 | metamorphic rock | 72 | foam | water coatings |
| 33 | quartzit.eh6 | metamorphic rock | 73 | oil15465 | water coatings |
| 34 | schist.h3a | metamorphic rock | 74 | oil34792 | water coatings |
| 35 | schist.h6a | metamorphic rock | 75 | oil39076 | water coatings |
| 36 | schist.h7 | metamorphic rock | 76 | oil42667 | water coatings |
| 37 | slate.h1a | metamorphic rock | 77 | soilfl.oat | water coatings |
| 38 | slate.h2a | metamorphic rock | 78 | qtzfloat | water coatings |
| 39 | slate.h3 | metamorphic rock | 79 | oil35473 | water coatings |
| 40 | 0127 | soil (Spodosols) | 80 | qtz.hem | quartz |

TABLE III. The standard deviations of errors in surface temperature and emissivities retrieved with two approaches of the day/night LST algorithm.

| atmospheric profile | δT_{s-day} (°K) | $\delta T_{s-night}$ (°K) | $\delta \epsilon_{20}$ | $\delta \epsilon_{22}$ | $\delta \epsilon_{23}$ | $\delta \epsilon_{29}$ | $\delta \epsilon_{31}$ | $\delta \epsilon_{32}$ | $\delta \epsilon_{33}$ |
|--|----------------------------|------------------------------|------------------------|------------------------|------------------------|------------------------|------------------------|------------------------|------------------------|
| with the statistical regression approach | | | | | | | | | |
| standard | 0.91 | 0.73 | 0.021 | 0.025 | 0.027 | 0.013 | 0.012 | 0.014 | 0.012 |
| A109 | 0.82 | 0.75 | 0.026 | 0.024 | 0.027 | 0.032 | 0.013 | 0.018 | 0.014 |
| A115 | 1.18 | 0.73 | 0.021 | 0.027 | 0.033 | 0.015 | 0.013 | 0.016 | 0.013 |
| standard-4K | 0.94 | 0.64 | 0.019 | 0.022 | 0.024 | 0.013 | 0.013 | 0.014 | 0.013 |
| with the χ^2 fit approach | | | | | | | | | |
| standard | 0.51 | 0.36 | 0.015 | 0.014 | 0.016 | 0.008 | 0.009 | 0.009 | 0.012 |
| A109 | 2.13 | 1.91 | 0.057 | 0.068 | 0.076 | 0.030 | 0.036 | 0.043 | 0.014 |
| A115 | 0.97 | 0.58 | 0.028 | 0.024 | 0.032 | 0.023 | 0.017 | 0.020 | 0.013 |
| standard-4K | 0.45 | 0.32 | 0.014 | 0.013 | 0.015 | 0.008 | 0.009 | 0.009 | 0.013 |

TABLE IV. The RMS errors in surface temperature and emissivities retrieved with the χ^2 fit approach of the day/night LST algorithm in the sensitivity study on assumptions of surface optical properties in conditions of $T_{a-day}=298.2^\circ\text{K}$, $T_{a-night}=290.2^\circ\text{K}$, $c_{wv}=2.6\text{cm}$, $\alpha=1.0$, $NE\Delta T=0.05-0.12^\circ\text{K}$, and systematic calibration error = 0.5%.

| test no. | test conditions | δT_{s-day} ($^\circ\text{K}$) | $\delta T_{s-night}$ ($^\circ\text{K}$) | $\delta\epsilon_{31}$ (daytime) | $\delta\epsilon_{32}$ |
|-------------|--|--|--|------------------------------------|-----------------------|
| C1 | $\epsilon_n(j)=\epsilon_d(j)$ $f_1=f_2=f_3$ Lambertian surface | 0.51 | 0.36 | 0.009 | 0.009 |
| C2 | $\epsilon_n(j)=\epsilon_d(j)+0.01$ | 0.75 | 0.55 | 0.013 | 0.013 |
| C3 | $\epsilon_n(j)=\epsilon_d(j)+0.1(1-\epsilon_d)$ | 0.51 | 0.41 | 0.009 | 0.009 |
| C4 | $f_2=0.95f_1$, $f_3=0.90f_1$ | 0.71 | 0.58 | 0.012 | 0.011 |
| C5 | $f_1=1.10f_3$, $f_2=1.05f_3$ | 0.68 | 0.60 | 0.011 | 0.011 |
| C6 | non-Lambertian surface (80%) | 0.61 | 0.43 | 0.011 | 0.010 |
| C7 | non-Lambertian surface (120%) | 0.58 | 0.41 | 0.010 | 0.010 |

TABLE V. The dependences of standard deviations (δT_s) and maximum errors (ΔT_s) in surface emissivities and temperatures retrieved with the χ^2 fit approach of the day/night LST algorithm on NE Δ T and calibration errors.

| test no. | NE Δ T ($^{\circ}$ K) | calibration errors (%) | δT_{s-day} ($^{\circ}$ K) | $\delta T_{s-night}$ ($^{\circ}$ K) | ΔT_{s-day} ($^{\circ}$ K) | $\Delta T_{s-night}$ ($^{\circ}$ K) | $\delta \epsilon_{31}$ | $\delta \epsilon_{32}$ |
|-------------|------------------------------------|---------------------------|---------------------------------------|---|---------------------------------------|---|------------------------|------------------------|
| D1 | 0.05,0.07,0.07,0.05,0.05,0.05,0.12 | 0.00 | 0.41 | 0.31 | 3.3 | 2.6 | 0.007 | 0.007 |
| D2 | 0.05,0.07,0.07,0.05,0.05,0.05,0.12 | 0.50 | 0.51 | 0.36 | 3.2 | 2.1 | 0.009 | 0.009 |
| D3 | 0.10,0.14,0.14,0.10,0.10,0.10,0.25 | 0.50 | 0.69 | 0.49 | 3.7 | 2.2 | 0.011 | 0.012 |
| D4 | 0.05,0.07,0.07,0.05,0.05,0.05,0.12 | 0.75 | 0.58 | 0.40 | 3.3 | 2.1 | 0.010 | 0.011 |
| D5 | 0.05,0.07,0.07,0.05,0.05,0.05,0.12 | 1.00 | 0.66 | 0.45 | 4.4 | 2.5 | 0.012 | 0.012 |

Thermal Infrared (3–14 μ m) Bidirectional Reflectance Measurements of Sands and Soils

William C. Snyder, Zhengming Wan, Yulin Zhang, and Yue-Zhong Feng

6832 Ellison Hall

Institute for Computational Earth System Science

University of California

Santa Barbara, CA 93106

submitted April 23, 1996, revised July 19, 1996

Phone: (805) 893-7353

ABSTRACT

Recent day/night land surface temperature (LST) algorithms can recover both emissivity and temperature, but require some assumptions about the relative optical properties of natural materials in the thermal infrared. We constructed a goniometer and measured the spectral, angular emissivity and bidirectional reflectance of sands and soils in the 3-14 μm range. In this paper we present the results for five diverse surfaces and examine the validity of the LST assumptions. We conclude that the change in emissivity with angle was small across the entire range for all of the materials except sand. In addition, for all of the materials, the measured variation in bidirectional reflectance anisotropy with wavelength was small enough to neglect.

I. INTRODUCTION

The optical properties of sands and soils in the thermal infrared (3 to 14 μ m) are needed for the remote sensing of surface temperature (Wan and Dozier, 1989) and in models of surface energy budget (Norman et al., 1995). A fundamental optical characterization of a diffuse material is its spectral, bidirectional reflectance distribution function (BRDF) at all incident and reflected angles. The integrated BRDF provides physical quantities such as angular, directional-hemispherical reflectance, and from Kirchhoff's law, the angular emissivity. Measurement of spectral BRDF in the thermal bands, however, is problematic. Previous studies in the thermal infrared have measured spectral and angular reflectance of sands and soils (Labed and Stoll, 1991), near-nadir spectral reflectance (Salisbury and D'Aria, 1992b; Salisbury and D'Aria, 1994), and non-spectral bidirectional reflectance (Becker et al., 1985). For the present study we designed and constructed a goniometer that provides high-resolution spectral BRDF from 3 to 14 μ m (Snyder and Wan, 1996). These measurements were made to support improved land surface temperature (LST) algorithms for the NASA MODIS satellite instrument (Solomonson et al., 1989). In particular, proposed day/night LST methods for NOAA AVHRR and MODIS (Li and Becker, 1993; Wan and Li, 1996) require some assumptions about the BRDF anisotropy that have not been verified. These day/night LST methods are valuable because they can recover both temperature and emissivity.

Most satellite sea and land surface temperature algorithms are based on variations of the split-window method, that applies the radiance in two or more thermal bands of a multi-spectral sensor to eliminate the atmospheric effects and extract the surface radiance. There are many recent improvements to split window methods for LST (Kerr et al., 1992;

Prata, 1994; Wan and Dozier, 1996). All such methods require accurate knowledge of the surface emissivity to convert the radiance to surface temperature. Better than 0.3K accuracy is possible for water because of the uniformity and predictability of the surface properties. Over land, the errors in emissivity significantly reduce the temperature accuracy. Specifically, over vegetation, the split-window accuracy is about 1.0K, but is considerably worse over bare soils (Kerr et al., 1992). Errors in emissivity are small for medium to dense vegetation canopies because multiple scattering and the relatively low component reflectance cause the overall emissivity to approach unity. In semi-arid and arid regions for which the viewed component of sand or soil increases, the accuracy of the estimated emissivity will be poorer. For these surfaces there is strong variability in emissivity caused by subtle changes in material composition and surface properties.

Because of this it will be difficult to achieve the MODIS LST error goal of 1.0 K over bare soils. This accuracy would require a comprehensive database of soil emissivities and an accurate land cover classification with high spatial and class resolution. The classification would also need to include temporal meteorological changes that affect surface moisture because this changes the emissivity (Salisbury and D'Aria, 1992a). Neither a complete database nor the classification are available. Consequently, there has been much effort devoted to alternative LST methods which can recover temperature without *a priori* knowledge of the emissivity.

Surface temperature from one multiband measurement is well known to be an underdetermined problem, even if atmospheric effects can be corrected by the use of independent measurement data. Success has been reported in recovering relative emissivity spectra for

mineralogical classification, etc., (Becker and Li, 1990). The extension of relative spectra to absolute emissivity and temperature is made possible by assuming at least one emissivity-related absolute value (Khale and Alley, 1992; Kealy and Hook, 1993). On the other hand, for the same surface measured at two temperatures, say, in day and night, both the daytime and nighttime temperatures and the band-averaged emissivities can be recovered. For the total number of variables to be reduced, the day-night algorithms still must make some assumptions about the band-to-band relation of the normalized BRDF of the surface. Because these involve relative properties, however, they will hold over a wider range of actual conditions. In this article we will present measurements of some sands and soils and evaluate the validity of these assumptions.

II. LST ALGORITHM REQUIREMENTS

With a single, n -band measurement we have n observations and n unknown emissivities. There is also the unknown surface temperature and additional atmospheric unknowns that are required to find the upwelling atmospheric radiance, the downwelling irradiance, and the atmospheric transmissions. In contrast, with daytime and nighttime measurements there will be a large surface temperature difference but constant emissivities, and we have $2n$ observations, so in principle we can solve for the two temperatures, the n emissivities, and an additional $2n - (n + 2)$ unknowns (Watson, 1992). The proposed MODIS day/night LST algorithm uses the seven bands shown in Table 1.

Because the reflected thermal and scattered solar downwelling irradiances are small with respect to the surface thermal radiance, we can link them to the downwelling irradiance with

the surface reflectance by the use of the Lambertian approximation. The radiance at the detector, L_i , for a particular geometry and spectral band, i , is then:

$$L_i = t_1(i)\varepsilon_i B_i(T_s) + t_2(i)(1 - \varepsilon_i)\frac{E_d(i)}{\pi} + t_3(i)f_i E_s(i) + L_u(i). \quad (1)$$

All terms are band-averaged quantities including the Planck radiance, $B(T_s)$. Here, T_s is the surface temperature, ε_i is emissivity and f_i is the BRDF of the surface. With the day and night atmospheric temperatures and column water vapors we can apply atmospheric models to predict the band averaged transmissions weighted by the in-band spectral properties of each term, $t_1(i)$, $t_2(i)$, and $t_3(i)$. Similarly, we can find the thermal and scattered solar downwelling irradiance, $E_d(i)$, the direct solar irradiance, $E_s(i)$, and the atmospheric upwelling radiance, $L_u(i)$. The direct solar term is non-zero only for the three mid-infrared bands (bands 20, 22, and 23) during daytime measurements, so three of the seven daytime equations require BRDF values. For a given geometry, we would like to reduce these three BRDF values to one non-spectral factor that is scaled by the spectral band reflectance (already related implicitly to emissivity).

Therefore, if we define this anisotropy factor as:

$$\alpha = \frac{\pi f}{(1 - \varepsilon)}, \quad (2)$$

and assume it is independent of the band, i , Equation (1) becomes:

$$L_i = t_1(i)\varepsilon_i B_i(T_s) + \frac{(1 - \varepsilon_i)}{\pi} [t_2(i)E_d(i) + \alpha t_3(i)E_s(i)] + L_u(i). \quad (3)$$

The seven MODIS LST bands will give seven equations for the day and seven for the night. The unknowns are the seven emissivities, one non-spectral anisotropy value, and the day and night surface temperatures. Simulations are applied to find the remaining unknowns from

the day and night column water vapors and air temperature parameters. Therefore, there are a total of 14 equations and 14 unknowns. Least-squares fitting methods may be applied to solve for the desired variables. Our simulations in wide ranges of surface emissivities and atmospheric conditions have shown that we can recover accurate surface temperatures if the following assumptions hold. Details of this day/night algorithm may be found in Wan and Li (1996).

We have assumed that there is one surface emissivity for each band and a single temperature within a given pixel for each measurement. For mixed pixels, the recovered emissivities will be averaged values and the recovered temperature will be the value from averaged radiance. In addition, although surface emissivity may vary with different view angles and changes in the surface properties between the day and night measurements, we have assumed that the variations are small. Finally, we have assumed that the anisotropy variations among the mid-infrared MODIS bands is small. We will show by theory and measurements that the angular change in emissivity can usually be neglected, and that the three mid-infrared BRDF values can be reduced to one constant non-spectral anisotropy scaled by the spectral reflectance.

III. MODEL ESTIMATES

There are several effects that could change the anisotropy with wavelength. For wavelengths near the soil particle size, the scattering physics lies in the range commonly called the resonance region, in which the complete wave nature of the incident radiation must be considered in the solution of scattering phase functions (Barber and Yeh, 1975). The change

in anisotropy caused by scattering physics is difficult to model because natural soil particles are rough, not spherical, and have a range of sizes. Therefore, for our approximation, we will consider only the effects of a change of the particle single-scattering reflectance with wavelength. As the single-scattering reflectance changes, the portion of the phase function caused by multiple scattering will change nonlinearly. This will change the normalized shape of the BRDF. One model that accounts for such multiple scattering is a particulate model originally developed for extraterrestrial studies (Hapke, 1981) and subsequently applied to terrestrial sands and soils in the visible and near infrared (Pinty, 1989; Ahmad, 1992; Jacquemond, 1992). Follow-on work improves this model (Liang, 1996), but we apply a simpler form here to estimate the variation in anisotropy with reflectance and the variation in emissivity with view angle.

Following Pinty (1989), the BRDF model is:

$$f = \frac{\rho_0}{4\pi \cos \theta_i + \cos \theta_r} ([1 + B(\xi)] P(\xi) + H(\theta_i, \rho_0)H(\theta_r, \rho_0) - 1), \quad (4)$$

Here, θ_i , θ_r are the incident and reflected zenith angles respectively, and ρ_0 is the single-scattering reflectance of the component particles. The scattering angle at a relative azimuth, ϕ , is:

$$\xi = \arccos(\cos \theta_i \cos \theta_r + \sin \theta_i \sin \theta_r \cos \phi). \quad (5)$$

The phase function $P(\xi)$ is approximated by a polynomial with empirical parameters, b , and c :

$$P(\xi) = 1 + b \cos \xi + c \frac{3 \cos^2 \xi - 1}{2}. \quad (6)$$

The backscattering function is:

$$B(\xi) = \frac{S(0)}{\rho_0 P(0)} \frac{1}{1 + (1/h) \tan(\xi/2)}, \quad (7)$$

where $S(0)$ is a parameter. Finally the $H(\xi)$ functions in the multiple-scattering term are approximated by:

$$H(\theta, \rho_0) = \frac{1 + 2 \cos \theta}{1 + 2 \cos \theta \sqrt{1 - \rho_0}}. \quad (8)$$

Based on our measured data, we chose a set of round numbers that represented a range of materials over a range of wavelengths: $h = 0.1$, $S(0) = 1.0$, $b = 0.5$, and $c = 0$. Use of these approximate values is acceptable because we only wish to estimate relative variations. The model was evaluated with the single-scattering reflectance set to $\rho_0 = 0.3$ and then changed to $\rho_0 = 0.2$. This corresponds to the largest spectral change in surface reflectance we have measured among the MODIS bands 20, 22, and 23. Numerically integrating the results for both settings gave the directional-hemispherical reflectance, which was then used to normalize the BRDF to give the anisotropy.

Figure 1 shows a section of the modeled anisotropy curve in the 30-degree azimuth plane with an incident angle of 32 degrees (0.55 radians on the positive zenith axis). Clearly the difference between the two curves for $\rho_0 = 0.3$ and $\rho_0 = 0.2$ is small with respect to the overall variation. We evaluated the anisotropy variation over a realistic range of azimuth, and incident and reflected zenith angles. The RMS variation over the range was 4.8% and the maximum error was 9.5%. Because we used a large reflectance change, these values should be considered upper bounds for typical materials.

The same model provided the relative change in emissivity with view angle. For the 3-5 μm region, we set $\rho_0 = 0.3$, the ratio of the emissivity at 53 degrees view zenith to that at 10 degrees was 0.986. For the 8-14 μm region we set $\rho_0 = 0.1$, and the ratio was 0.996. These ratios are stronger functions of the chosen parameters than the anisotropy change

and therefore are less reliable estimates. These modeled values support the LST algorithm assumptions of small spectral dependence in anisotropy and small angular dependence in emissivity.

IV. MEASUREMENTS

Measurements of spectral reflectance in the thermal region are difficult because natural materials often have a very low reflectance. Active reflectance measurement requires a source, and a wideband source both illuminates and heats the sample, causing a radiance change that is a combination of the surface reflection and thermal emission. In previous studies, one system measured the wideband thermal infrared BRDF by detecting the radiance change from modulating a wideband infrared source based on a heated SiC element (Becker et al., 1981; Becker et al., 1985). A $10.6\text{ }\mu\text{m}$ CO₂ laser was also used as a narrowband source. The modulation method reduces the effects of surface heating and cancels the unchanging background contribution. Other systems applied the emissive technique with a heated sample to measure spectral emissivity at nadir with the box method (Nerry et al., 1990) and to characterize the dependence of spectral emissivity on angle with a mirror system (Labeled and Stoll, 1991). All of these instruments were employed to study soil and sand properties. With our spectral infrared bidirectional reflectance and emissivity (SIBRE) instrument, the thermal infrared source is a heated ceramic plate, and we measure reflected radiance with a Fourier transform spectrometer that responds in the $3\text{--}14\text{ }\mu\text{m}$ range. Both of these are mounted on a pointing system that affords a wide range of geometrical combinations over the sample hemisphere. Because of the practical aspects of Fourier scanning, we use slow-speed

source chopping to eliminate the background radiance and instrument offsets. The surface temperature change caused by the source is significant, and is corrected by curve-fitting the detected radiance for each source state (Snyder and Wan, 1996). A four-step differential-ratio method is used to cancel the background, instrument calibration, and source temperature terms. Our system is unique because it measures hyperspectral BRDF across the thermal infrared over a wide range of source and detector angles. Moreover, it can measure rougher surfaces because it has a larger spot size (~ 5 cm diameter) than integrating sphere systems (< 1 cm). The resulting measurements may be integrated over angle or wavelength to give surface properties tailored for a specific satellite sensor.

True BRDF is a differential quantity, but if it is smooth it can be approximated with bidirectional reflectance measurements. The SIBRE spectrometer measures the reflected radiance inside a solid angle of approximately one milli-steradian. The source produces wideband infrared irradiance on the surface from a solid angle of 43 milli-steradians. Figure 2 shows the source zeniths and relative azimuths, and the set of five detector zenith angles that are repeated for each source position. The source zenith angle ranges from 2 to 70 degrees, the detector angle ranges from 10 to 53 degrees. The relative azimuth ranges from 30 to 180 degrees with a step size that depends on the source zenith. The total number of combinations is 187, but we also measure diffuse materials with a subset of 45 geometries. We have characterized several diffuse materials with both 45 and 187 geometrical combinations and obtained almost the same results. At each geometry we record spectra sampled at 2 cm^{-1} intervals over a useful range of 700 to 2800 cm^{-1} .

Further details of the SIBRE instrument and the recovery of BRDF from radiance mea-

measurements are given by Snyder and Wan (1996). The BRDF spectra for each material are filtered with a 7-bin median and 7-bin moving average. The averaged data are also filtered spatially by the weighting kernel $k = \cos^n(\cdot)$ for both the incident and reflected directions. Here, k is zero when the argument is larger than $\pi/2$ and we determined that for the subset of 45 geometries, a value of $n = 11$ filters the sampling but preserves the salient features of the BRDF. Moreover, Hemholtz reciprocity (Nicodemus, 1967) is imposed on the BRDF by averaging the two reconstructed values that result from switching the incident and reflected zenith angles at the same relative azimuth. What we report is thus the true BRDF filtered by convolution with the finite source and detector angles, and by convolution with the reconstruction kernel.

We checked our BRDF values by measuring reflectance with an integrating sphere over the same spectral range. These measurements are compared with the integrated BRDF from the SIBRE. For the integrating sphere, we apply a four-step differential-ratio method based on a calibrated, sintered gold standard reference. Measurements of water on the integrating sphere exhibit systematic reflectance errors of less than 0.002 across the spectrum when compared to Fresnel theory. Water has a low reflectance: approximately 0.01-0.03 in the 3-14 μm range. The integrating sphere was then used as a reference to check the bias in the SIBRE measurements. For the low-reflectance materials near 800 cm^{-1} , the mean difference between the integrating sphere and the SIBRE reflectance was 0.005. For the higher reflectance regions near 2500 cm^{-1} the mean difference was 0.02. The standard deviation of the differences was 0.003 and 0.012 respectively. These errors include not only the error in instrument calibration, but also errors caused by temporal variations in the illumination

and hemispherical response weighting. It should be noted that there are differences in the response of the instruments to a backscattering lobe, which commonly occurs with natural materials. Finally it should be noted that the bias errors tend to cancel in the computations of the relative quantities of interest here.

Spectral BRDF measurements of 15 sands and soils with different compositions and surface textures produced a wide range of reflectances and anisotropies. The five materials presented here represent the extremes and are summarized in Table 2. The organic soil is decomposing soil litter that was very dark brown with a coarse surface. It was air dried only, and remained somewhat moist during measurements. The sand is beach sand that was screened, washed in distilled water, and air dried. Next is a sample of screened silt loam soil from Lincoln county, Kentucky. Although not technically so, we will call this "silt." This had a few dry grass pieces and was reported to have 3% carbon content with various other minerals. It was one of nine obtained from National Soil Survey Center in Lincoln, Nebraska. After processing, screening, and drying, the Soil Survey Center samples are archived primarily for composition studies. For a more volumetric surface, we placed pieces of green grass and dry leaves over a sample of the organic soil so that it was approximately 40% covered. Finally, the gravel sample is a light tan mollisol from a grassy area in Santa Barbara, California. This material had a large range of particle sizes, but we eliminated the sand and silt in this sample smaller than 2mm by screening. The remaining gravel included some organic content and dust.

V. RESULTS AND DISCUSSION

The BRDF measurements of the materials were numerically integrated to provide the spectral directional-hemispherical reflectances that are presented in Figure 3. These curves correspond to a 10-degree view angle. The seven reference lines correspond to the seven MODIS band centers. Note that from approximately 1300 cm^{-1} to 1900 cm^{-1} and in a small region around 2350 cm^{-1} there is strong atmospheric attenuation. The measurements in these regions are less accurate because the SIBRE has a path length of $\sim 3\text{ m}$. In the thermal infrared, the reflectance variability depends strongly on the organic content, with the sand having the highest peaks and the organic soil having the lowest. Complete descriptions of the reflectance features for many materials are available (Salisbury and D’Aria, 1992a; Salisbury and D’Aria, 1992b; Salisbury and D’Aria, 1994). Figure 4 shows the 8-14 μm region with the ordinate changed to emissivity. The set of five dissimilar samples of sands and soils exhibit a uniformly high emissivity for wavelengths longer than $10.5\text{ }\mu\text{m}$ ($0.96 - 0.995$). This agrees with the box method measurements by Nerry et al. (1990). Even without the sand sample, however, emissivity variations in the 8-14 μm region bands exceed 0.01.

To validate our assumptions for LST algorithms, we examined the spectral, angular change of the five emissivities. The difference between the day and night look angles for one or several MODIS instruments can exceed 60 degrees, but this extreme is unlikely. Figure 5 shows the ratio of the emissivity at 53 degrees to that at 10 degrees for the five materials. The four soil materials change less than one percent across the spectrum. Sand showed larger variations, which compare closely with those from previous angular emissivity studies (Labeled and Stoll, 1991). In the case of bare sand, the emissivity variations with angle may

not be small enough to neglect for LST applications.

Next, we compare the anisotropies of the materials. Figure 6 shows these in the same geometry that was used in the model estimate. The values are band-averaged at $4.06 \mu\text{m}$ (2460 cm^{-1}) corresponding to MODIS band 23. The soils exhibit backscattering peaks of various magnitudes as expected from models and measurements in the near infrared and visible (Ahmad and Deering, 1992; Roujean et al., 1992). The soil and vegetation mix displays a volumetric scattering characteristic as predicted by Roujean et al. (1992) with a minimum near nadir and larger values at extreme angles. Sand has a small amount of back and forward scattering and is the most isotropic of the materials, as was determined by Becker et al. (1985) in the $8\text{-}14\mu\text{m}$ range. Note that if we did not account for the anisotropy in the LST algorithm and instead used the reflectance with the Lambertian assumption, the error in the reflected direct solar term would be higher than 10% for some of the materials.

Figures 7 through 11 show these anisotropy curves at each of the three MODIS bands of interest. Ideally, there would be no differences among the curves for a given material. It is clear that the anisotropy is different for different materials, but stays quite constant across the $3.5\text{-}4.2 \mu\text{m}$ range for each of the five samples. As was done for the model, we computed RMS and maximum variation for the 45 measured geometries between the band 23 anisotropy values and those for bands 22 and 20. The results are summarized in Table 3. The RMS variations are approximately 1-3% and the maximum variations are 2-7%.

VI. SUMMARY AND CONCLUSIONS

The measurements presented in this paper further the knowledge of the optical properties of terrestrial materials in the thermal infrared. The results support some assumptions required for recent day/night LST algorithms. In particular, we determined that the change in emissivity between 10 and 53 degrees was small: less than 1% for all materials tested except sand. From simulations we have concluded that a change of this size is acceptable in the seven-band day/night LST algorithm. For bare sand, the change ranged up to 4% in the 8-10 μm region and was approximately 2% in the 3-5 μm and 10-14 μm regions. Consequently, angular emissivity effects need to be considered to achieve high LST accuracies with sand.

In addition, we examined the BRDF of the samples in the 3-5 μm range where the reflected solar irradiance is significant. The BRDF exhibits the same characteristics that appear in other studies of these materials. Our model estimates indicated only a small change in BRDF anisotropy with wavelength. We confirmed by measurements that variation in the anisotropy was 1-2% RMS among the MODIS bands 20, 22, and 23. This is low enough to assume it is constant for the proposed day/night LST algorithm.

Ideal samples would be unprocessed, undisturbed sections of natural surfaces. This would preserve the structure and weathering that can affect optical properties. Of course, such samples are more difficult to collect and measure. Although they are processed, we feel that the samples we used demonstrate the salient properties of natural surfaces. This is true particularly for the bare surfaces where the day/night approach is most useful. For future work concerning absolute optical properties, we plan to collect and measure unprocessed samples.

VII. ACKNOWLEDGMENTS

This work was supported by Earth Observing System Program contract NAS5-31370 of the National Aeronautics and Space Administration. We would also like to thank the reviewers for helpful comments.

References

Ahmad, S.P., and Deering, D.W. (1992), A simple analytical function for bidirectional reflectance, *J. Geophys. Res.* 97:18,867-18,886.

Barber, P. and Yeh, C. (1975), Scattering of electromagnetic waves by arbitrarily shaped dielectric bodies, *Appl. Optics* 14:2864-2872.

Becker, F., Ngai, W., and Stoll, M.P. (1981), An active method for measuring thermal emissivities: Implications and perspectives for remote sensing, *Adv. Space Res.* 1:193-210.

Becker, F., Ramanantsizehena, P., and Stoll, M.P. (1985), Angular variation of the bidirectional reflectance of bare soils in the thermal infrared, *Appl. Optics* 24:365-375.

Becker, F., and Li, Z. (1990), Temperature-independent spectral indices in the thermal infrared bands, *Remote Sens. Environ.* 32:17-33.

Hapke, B. (1981), Bidirectional Reflectance Spectroscopy 1. Theory, *J. Geophys. Res.* 86:3039-3054

Jacquemoud, S., Baret, F., and Hanocq, J.F. (1992), Modeling spectral and bidirectional soil reflectance, *Remote Sens. Environ.* 41:123-132.

- Kahle, A.B. and Alley, R.E. (1992), Separation of temperature and emittance in remotely sensed radiance measurements, *Remote Sens. Environ.* 42:107-111.
- Kealy, P.S., and Hook, S.J. (1993), Separating temperature and emissivity in thermal infrared multispectral scanner data: implications for recovering land surface temperatures, *IEEE Trans. Geosci. Remote Sens.* 31:1155-1164.
- Kerr, Y.H., Lagouarde, J.P., Imbernon, J. (1992), Accurate land surface temperature retrieval from AVHRR data with use of an improved split window algorithm, *Remote Sens. Environ.* 41:197:209.
- Labed, J. and Stoll, M. (1991), Angular variation of land surface spectral emissivity in the thermal infrared: laboratory investigations on bare soils, *Int. J. Remote Sens.* 12:2299-2310.
- Li, Z., and Becker, F. (1993), Feasibility of land surface temperature and emissivity determination from AVHRR data, *Remote Sens. Environ.* 43:67-85.
- Liang, S. and Townshend, J.R.G. (1996), A modified Hapke model for soil bidirectional reflectance, *Remote Sens. Environ.* 55:1-10.
- Nerry, F., Labed, J., and Stoll, M.P. (1990), Spectral properties of land surfaces in the thermal infrared 1. Laboratory measurements of absolute spectral emissivity signatures, *J. Geophys. Res.* 95:7027-7044.

Nicodemus, F.E. (1967), In *Applied Optics and Optical Engineering* (R. Kingslake, Ed.), Academic Press, New York, Chap. 8 in Volume IV.

Norman, J.M., Divakarla, M., and Goel, N.S. (1995), Algorithms for extracting information from remote thermal-IR observations of the Earth's surface, *Remote Sens. Environ.* 51:157-168.

Pinty, B., Verstraete, M.M., and Dickinson, R.E. (1989), A physical model for predicting bidirectional reflectances over bare soil, *Remote Sens. Environ.* 27:273-288.

Prata, A.J. (1994), Land surface temperatures derived from the advanced very high resolution radiometer and the along-track scanning radiometer 2. experimental results and validation of AVHRR algorithms, *J. Geophys. Res.* 99:13025-13058.

Roujean, J., Leroy, M., and Dechamps, P. (1992), A bidirectional reflectance model of the Earth's surface for correction of remote sensing data, *J. Geophys. Res.* 97:20,455-20,468.

Salisbury, J.W. and D'Aria, D.M. (1992a), Infrared (8-14 μm) remote sensing of soil particle size, *Remote Sens. Environ.* 42:157-165.

Salisbury, J.W. and D'Aria, D.M. (1992b), Emissivity of terrestrial materials in the 8-14 μm atmospheric window, *Remote Sens. Environ.* 42:83-106.

Salisbury, J.W. and D'Aria, D.M. (1994), Emissivity of terrestrial materials in the 3-5 μm atmospheric window, *Remote Sens. Environ.* 47:345-361.

Snyder, W.C. and Wan, Z. (1996), Surface temperature correction for active infrared reflectance measurements of natural materials, *Appl. Optics* 35:2216-2220.

Salomonson, V., Barnes, W., Maymon, P., Montgomery, H., and Ostrow, H. (1989), MODIS: advanced facility instrument for studies of the Earth as a system, *IEEE Trans. Geosci. Remote Sens.* 27:145-153.

Wan, Z. and Dozier, J. (1989), Land-surface temperature measurement from space: physical principles and inverse modeling, *IEEE Trans. Geosci. Remote Sens.* 27:268-277.

Wan, Z. and Dozier, J. (1996), A generalized split-window algorithm for retrieving land-surface temperature measurement from space, *IEEE Trans. Geosci. Remote Sens.* 34:1-14 (in press).

Wan, Z. and Li, Z. (1996), A physics-based algorithm for retrieving land-surface emissivity and temperature from EOS/MODIS data, *IEEE Trans. Geosci. Remote Sens.* (revised).

Watson, K. (1992), Two-temperature method for measuring emissivity, *Remote Sens. Environ.* 42:117-121.

Table 1. MODIS Thermal Infrared Bands for LST

| Band No. | Spectral Range (μm) |
|-----------------|--|
| 20 | 3.66–3.84 |
| 22 | 3.93–3.99 |
| 23 | 4.02–4.08 |
| 29 | 8.4–8.7 |
| 31 | 10.8–11.3 |
| 32 | 11.8–12.3 |
| 33 | 13.2–13.5 |

Table 2. Descriptions of the Five Sample Materials

| Name | Description & Texture |
|-------------|----------------------------------|
| ORG_SOIL | organic compost (0.03–6 mm) |
| SAND | washed sand (0.3–1.0 mm) |
| SILT | screened soil (0.01–0.3 mm) |
| VEG_SOIL | compost with grass and leaves |
| GRAVEL | gravel (2–10 mm) |

Table 3. Percent Anisotropy Change for Bands 22 and 20 Relative to Band 23

| Sample | Band 22 | | Band 20 | |
|----------|---------|-------|---------|-------|
| | RMS | MAX | RMS | MAX |
| ORG_SOIL | 1.3 | 2.7 | 2.1 | 5.7 |
| SAND | 0.8 | 2.4 | 1.1 | 3.4 |
| SILT | 2.5 | 5.1 | 2.7 | 5.9 |
| VEG_SOIL | 1.5 | 2.9 | 3.3 | 6.8 |
| GRAVEL | 0.6 | 1.9 | 1.1 | 3.3 |
| Average | 1.3 % | 3.0 % | 2.1 % | 5.0 % |

List of Figures

1. Anisotropy change resulting from changing the single-scattering reflectance from 0.3 to 0.2 in the Hapke model. The plot is in the 30-degree azimuth plane with the angle of incidence at 32 degrees. Positive zenith values represent backscattering.
2. The detector declinations (triangles) and source positions (circles) for the BRDF measurements. The radial axis is linear in the zenith angle.
3. Spectral reflectance of the five sands and soils. Also shown are the center values of the MODIS bands of interest for land surface temperature.
4. Spectral emissivities of the five materials in the thermal infrared. The scale is set to show the variations in the four higher-emissivity materials in MODIS bands 31, 32, and 33.
5. Ratios of the angular emissivity at a 53-degree view angle to that at a 10-degree view angle.
6. Anisotropy of the five materials for MODIS band 23 in the 30-degree azimuth plane. The angle of incidence is 32 degrees. Positive zenith angles represent the backscatter direction.
7. Anisotropy of the organic soil in each of the three MODIS bands. The geometries are the same as for Figure 6.
8. Anisotropy variation for sand.
9. Anisotropy variation for silt.
10. Anisotropy variation for the soil/vegetation mix.
11. Anisotropy variation for gravel.

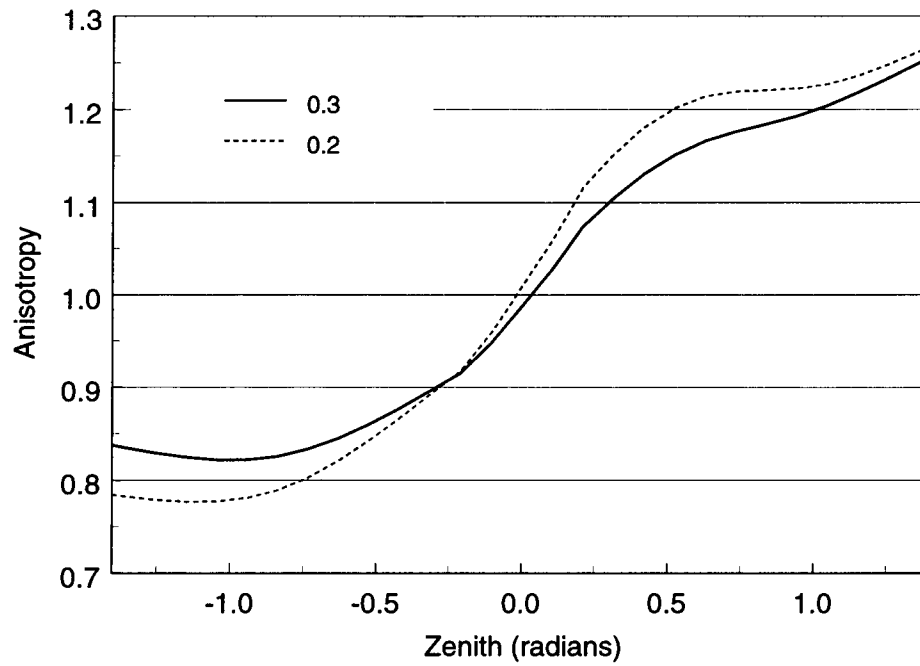


Figure 1: Anisotropy change resulting from changing the single-scattering reflectance from 0.3 to 0.2 in the Hapke model. The plot is in the 30-degree azimuth plane with the angle of incidence at 32 degrees. Positive zenith values represent backscattering.

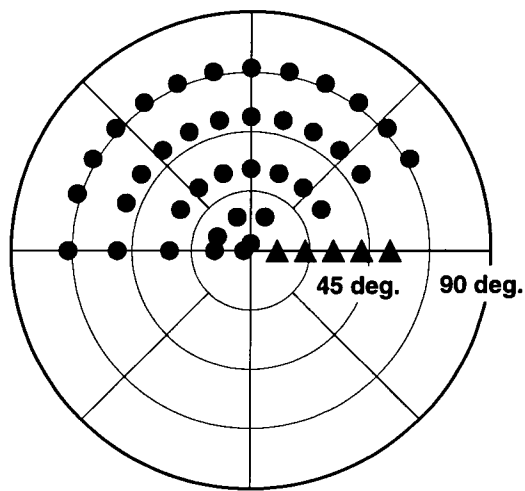


Figure 2: The detector declinations (triangles) and source positions (circles) for the BRDF measurements. The radial axis is linear in the zenith angle.

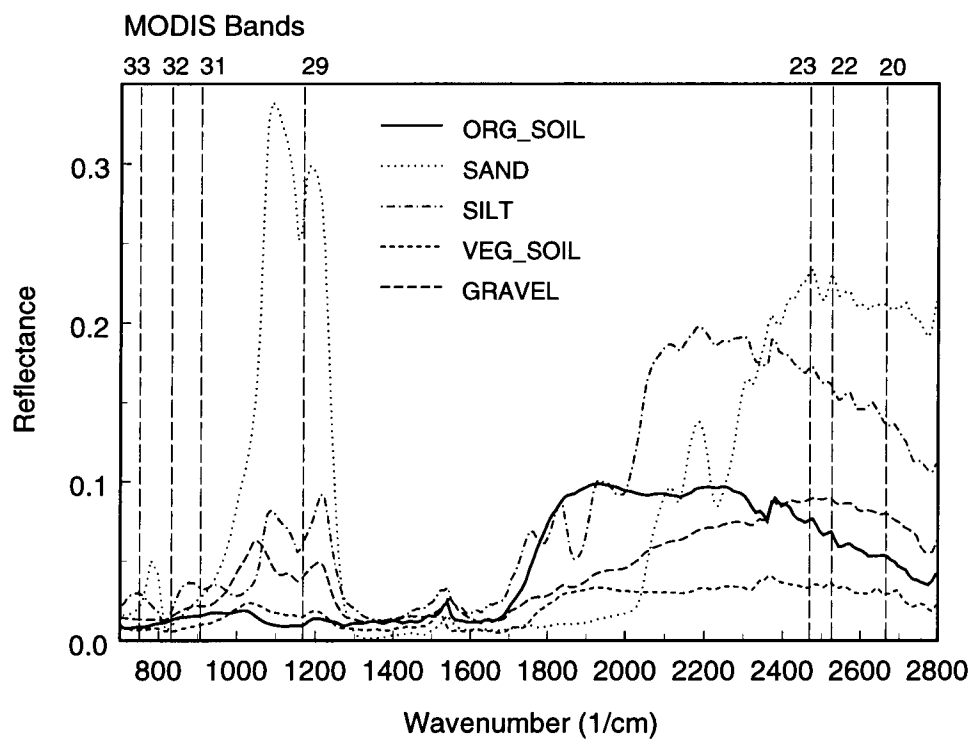


Figure 3: Spectral reflectance of the five sample materials. Also shown are the center values of the MODIS bands of interest for land surface temperature.

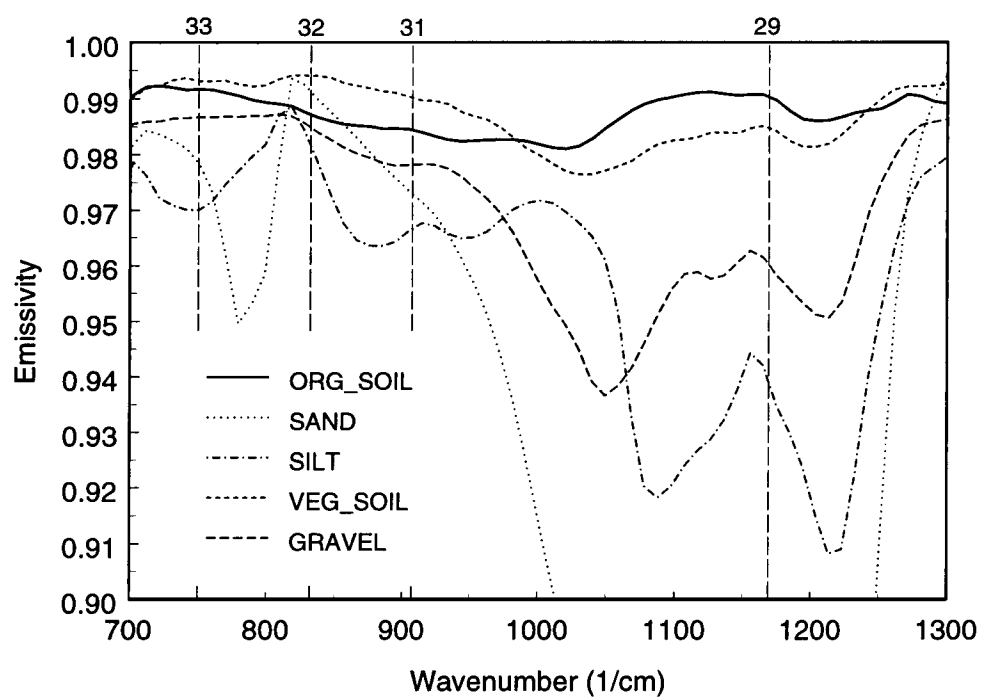


Figure 4: Spectral emissivities of the five materials in the thermal infrared. The scale is set to show the variations in the four higher-emissivity materials in MODIS bands 31, 32, and 33.

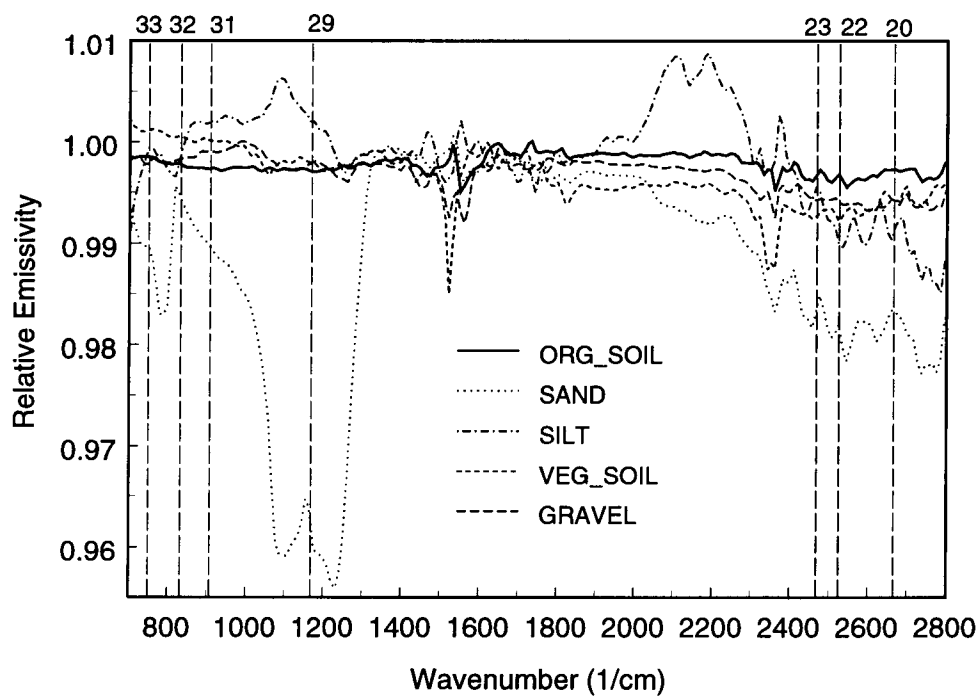


Figure 5: Ratios of the angular emissivity at a 53-degree view angle to that at a 10-degree view angle.

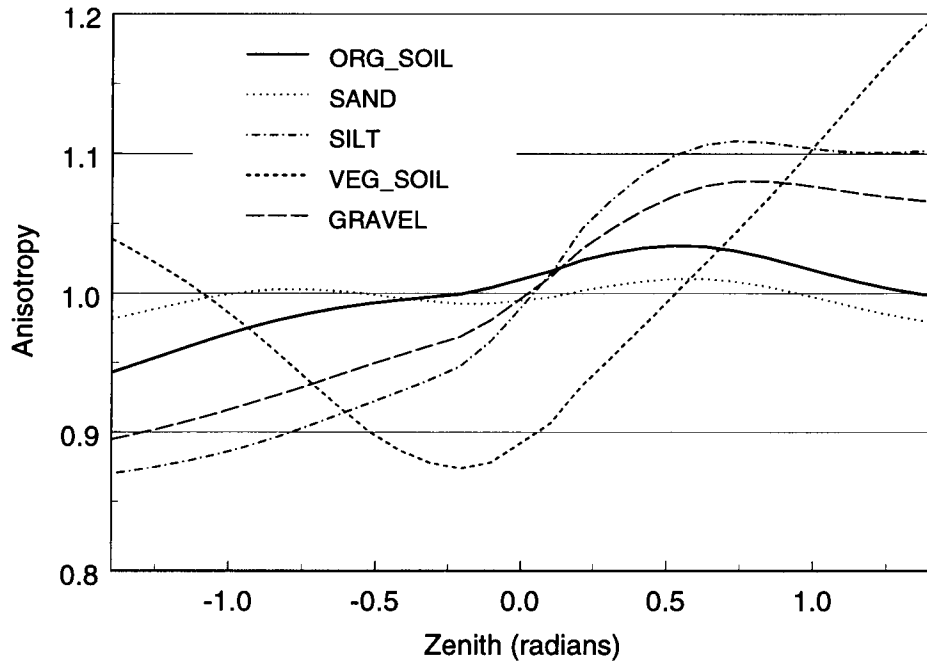


Figure 6: Anisotropy of the five materials for MODIS band 23 in the 30-degree azimuth plane. The angle of incidence is 32 degrees. Positive zenith angles represent the backscatter direction.

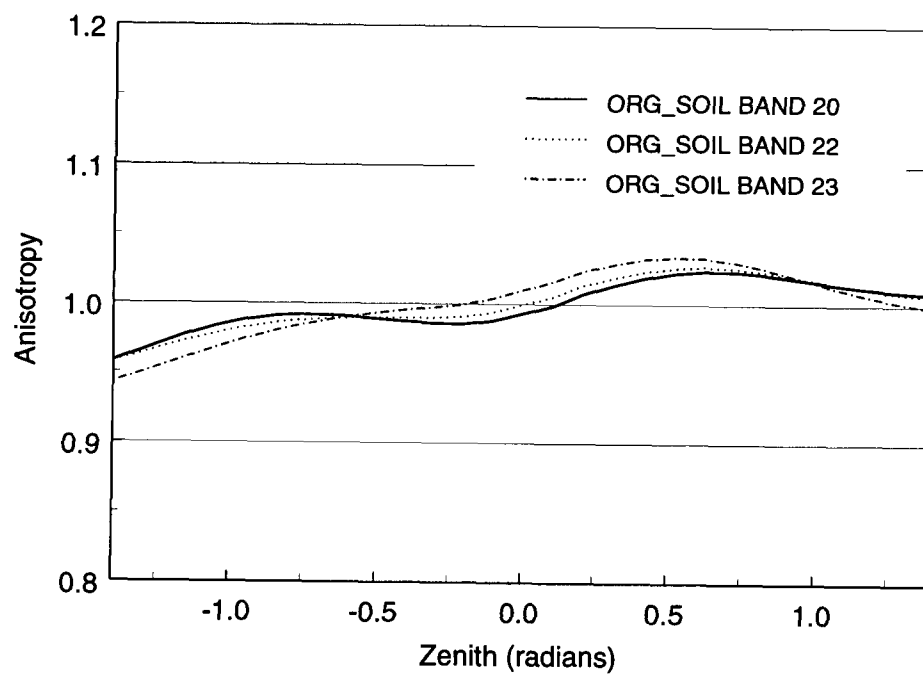


Figure 7: Anisotropy of the organic soil in each of the three MODIS bands. The geometries are the same as for Figure 6.

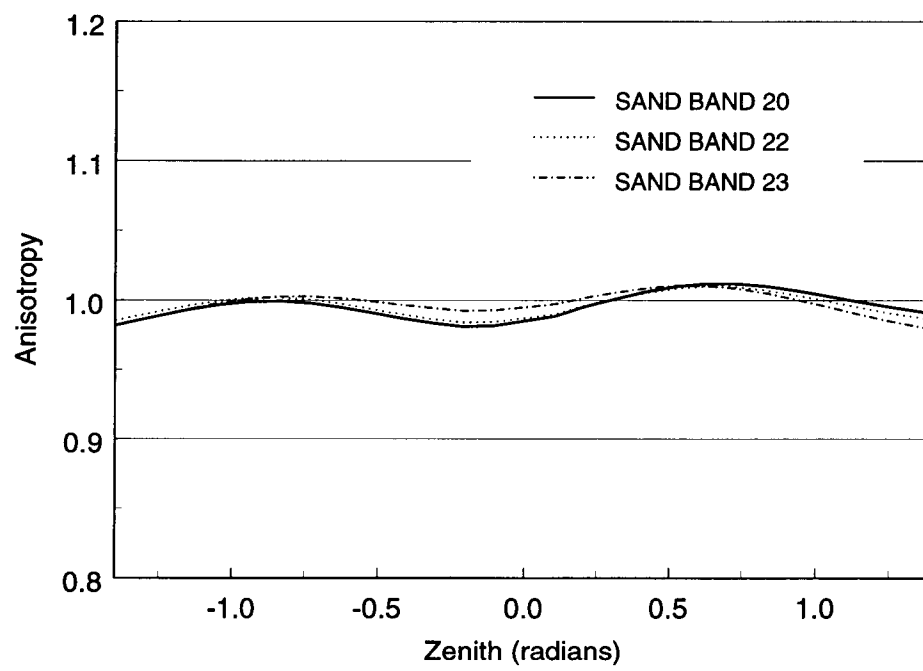


Figure 8: Anisotropy variation for sand.

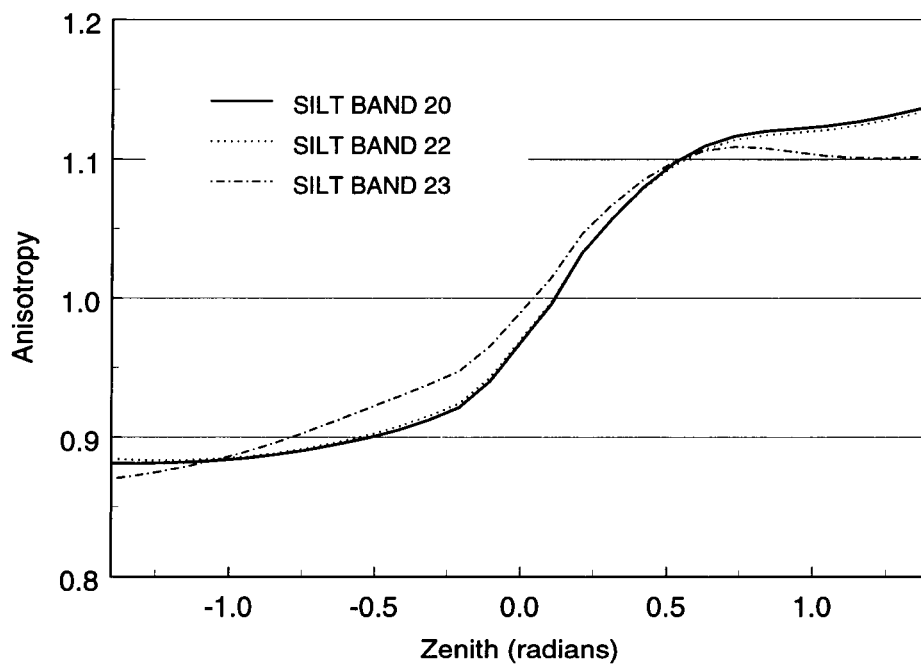


Figure 9: Anisotropy variation for silt.

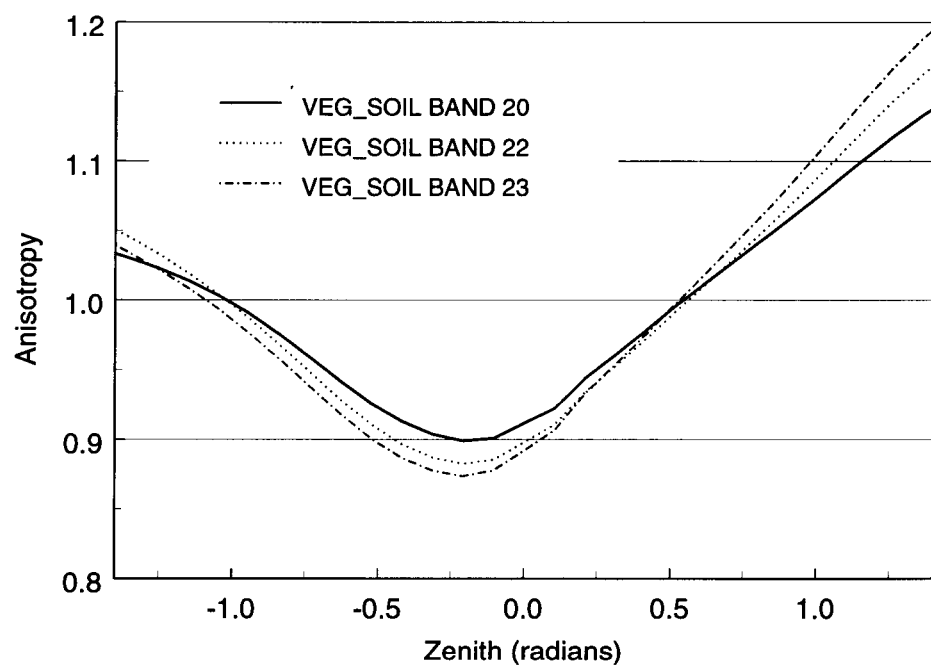


Figure 10: Anisotropy variation for the soil/vegetation mix.

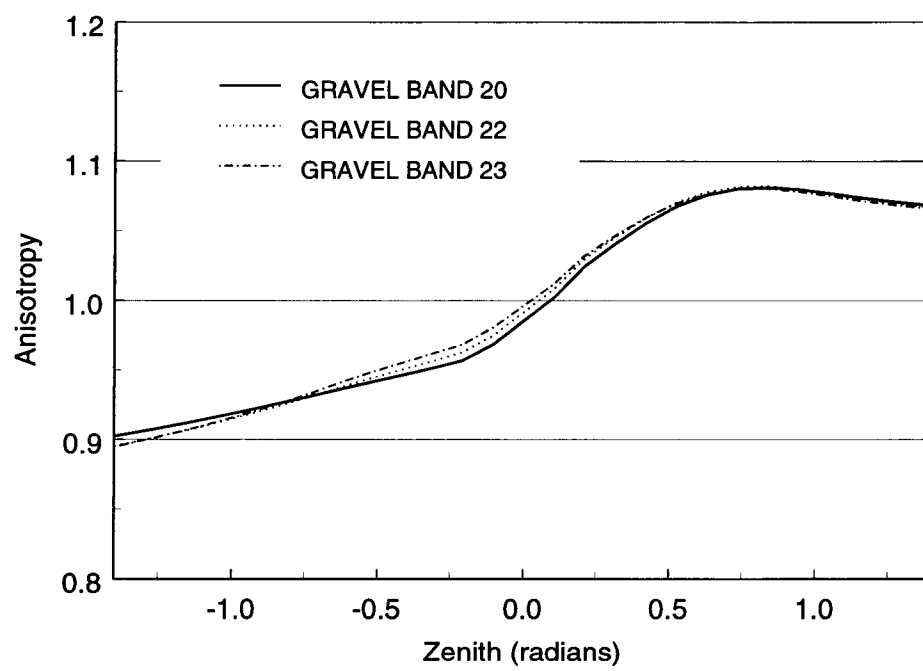


Figure 11: Anisotropy variation for gravel.